Numerical simulation of impulse wave generation by idealized landslides with OpenFOAM

M. Rauter [a,b,c,*], L. Hoße [a,d], R.P. Mulligan [e], W.A. Take [e], F. Løvholt [a]

[a] *Norwegian Geotechnical Institute, Department of Natural Hazards, Oslo, Norway*
[b] *University of Oslo, Department of Mathematics, Oslo, Norway*
[c] *University of Innsbruck, Institute of Infrastructure, Division of Geotechnical and Tunnel Engineering, Innsbruck, Austria*
[d] *University of Potsdam, Institute of Geosciences, Potsdam, Germany*
[e] *Queen's University, Department of Civil Engineering, Kingston, Canada*

ARTICLE INFO

ABSTRACT

Landslide tsunamis and impulse waves are hazardous events with severe socioeconomic impacts. A long standing problem with simulations of these events is the generation stage, where landslides and water interact. Depth-averaged models like the Saint-Venant or Boussinesq Equations lose their validity for such applications. Therefore, we have to rely on a full treatment of the hydrodynamics, for instance by applying the Navier-Stokes Equations and Computational Fluid Dynamics (CFD). However, applications of fully three-dimensional methods to landslide tsunamis are sparse, and have often been outperformed by depth averaged models when compared to experimental data. In this work, we evaluate the multiphase Navier-Stokes Equations as implemented in OpenFOAM® in terms of impulse wave generation. We focus on a simplified two-dimensional setup where the landslide consists of water, in order to circumvent additional complexities due to treatment of landslide rheologies. We conduct a thorough grid refinement study and compare results to experiments to investigate model convergence, stability, and accuracy. The simulations display good agreement with the experimental data if the Courant-Friedrichs-Lewy (CFL) condition is modified to account for the specific properties of the multiphase system. Further, we use the validated model for sensitivity studies and to review various scaling relations for landslide generated tsunamis. The application of numerical models allows us to perform broad parametric tests and dissect the underlying physics of these predictive equations systematically. We found that the first wave crest may be well estimated by solely the landslide mass in our setting. Including additional properties related to landslide momentum can improve the predictive skill, while other parameters lead to no substantial improvement.

1. Introduction

Landslides are the second most frequent tsunami source (Harbitz et al., 2014). Recently, the 2018 Anak Krakatoa landslide induced tsunami caused several hundred fatalities (e.g. Grilli et al., 2019). Several other landslide events of the last decade generated impulse waves with run-up heights of up to 150 m (e.g. George et al., 2017; Gylfadóttir et al., 2017; Paris et al., 2019). Landslide tsunamis have traditionally been modelled through depth-integrated (i.e., two-dimensional) models, reducing the complexity and improving the accuracy in comparison to fully three-dimensional models (e.g. Løvholt et al., 2015; Yavari-Ramshe and Ataie-Ashtiani, 2016). The assumptions of depth-integrated models fit well with the propagation stage of tsunamis and for some cases (e.g. submarine landslides, earthquakes) also to the generation stage. However, the generation can be influenced by a highly rotational and depth-varying velocity field, a complex water surface (e.g. breaking waves) and other processes that stand in strong contrast to the assumptions of depth-integrated and potential flow models. This is especially the case for tsunamis generated by subaerial landslides that impact the water reservoir, such as the Vajont landslide (e.g. Panizzo et al., 2005), the Ritter volcano eruption (e.g. Ward and Day, 2003) or the hypothetical La Palma island collapse (e.g. Gisler et al., 2006; Løvholt et al., 2008; Abadie et al., 2012). Moreover, depth averaged models have shown to face difficulties related to strong

---

* Corresponding author. Norwegian Geotechnical Institute, N-0855, Oslo, Norway.
E-mail addresses: matthias.rauter@ngi.no (M. Rauter), lhosse@uni-potsdam.de (L. Hoße), ryan.mulligan@queensu.ca (R.P. Mulligan), andy.take@queensu.ca (W.A. Take), finn.lovholt@ngi.no (F. Løvholt).

non-linearities (e.g. Løvholt et al., 2013) and steep topographies (Løvholt and Pedersen, 2009). For such cases, the most appropriate approach requires a minimum degree of simplification, which implies solving full three-dimensional continuum mechanical models, i.e. the Navier-Stokes Equations. Some studies couple three-dimensional models with depth-averaged models, either for landslides (Domnik et al., 2013), impulse waves (Løvholt et al., 2008) or other large scale flows, which are too extensive for a complete three-dimensional treatment (Mintgen and Manhart, 2018). For a comprehensive comparison the reader is refereed to these publications. Notably, a wide range of alternative and mixed methods was investigated: Savage-Hutter model coupled with Navier-Stokes Equations (e.g. Ma et al., 2015), discrete element method coupled with Navier-Stokes Equations (e.g. Shan and Zhao, 2014), smoothed particle hydrodynamics (e.g. Pastor et al., 2008; Heller et al., 2016) or particle finite element method (e.g. Mulligan et al., 2020) are a few of the promising approaches.

Modelling landslide tsunamis with the Navier-Stokes Equations implies solving a multiphase system. At least two phases, water and air are required to simulate surface water waves. In addition, the landslide should be treated as an individual phase, to take into account the respective properties. Turbulence, that cannot be resolved with the numerical method must be taken into account by the mathematical model. This issue is usually tackled with turbulence models, and especially the Reynolds-averaged Navier-Stokes (RANS) Equations in combination with the k-ε-model have become popular for practical applications (Launder and Spalding, 1974). In addition, the complex rheology of the granular and porous landslide must be adequately described. Various rheologies have been suggested (e.g. Jop et al., 2006; Boyer et al., 2011; Savage et al., 2014; Barker et al., 2017; Si et al., 2018a), however, a unified description of partially and fully water-saturated landslides is still too complex and too poorly understood for many applications. Furthermore, the porosity of granular materials leads to dynamic bulk density changes and excess pore pressure, substantially influencing the rheology (e.g. Ilstad et al., 2004; Rondon et al., 2011). Indeed, most studies with Navier-Stokes Equations rely on simplified rheologies (e.g. Newtonian or Herschel-Bulkley fluids) that do not consider the granular character and the porosity of landslides (e.g. Gisler et al., 2006; Abadie et al., 2010, 2012; Viroulet et al., 2013, 2016; Gabl et al., 2015; Kim et al., 2020). Others use rigid bodies to simulate landslides and similar objects (e.g. Heinrich, 1992; Liu et al., 2005; Chen et al., 2020; Romano et al., 2020). Si et al. (2018b) is one of the few examples of combining a surface wave model and granular flows in terms of Navier-Stokes Equations.

In the present numerical study, we will omit the complex nature of the landslide to focus solely on the tsunami generation and propagation. This way we avoid possible shortcomings in the treatment of the landslide, artificially impacting the wave generation and leading to a less transparent analysis. We are guided by the experiments of Bullard et al. (2019), where the landslide was pure water in contrast to many other experiments, where granular materials were used (e.g. Viroulet et al., 2013; Fritz, 2002). The rheology of the landslide is hence described fairly well by a simple Newtonian fluid in combination with the turbulence model.

The goal of this work is to verify and validate the multiphase solver of the open source CFD toolkit OpenFOAM® (OpenCFD, 2018) in terms of impulse wave generation and propagation. In particular, we are able to demonstrate that the criterion for adaptive time stepping in Open-FOAM, known as Courant-Friedrichs-Lewy (CFL) condition (see section 2.2), is insufficient for the presented cases and we introduce a better performing extension. We compare results to the experimental observations of Bullard et al. (2019), showing that the numerical model is able to reproduce the experimental results without any parameter fitting.

In a further step, the verified and validated model is applied for a sensitivity and scaling analysis that goes beyond the experimental results. Numerical simulations allow a high degree of automation and even the tank geometry can be modified with little effort. This enables us to

investigate a large variety of still water depths and impact angles. We test a wide range of semi-empirical and theoretical scaling relations (Fritz, 2002; Heller and Hager, 2010; Zitti et al., 2015; Mulligan and Take, 2017; Bullard et al., 2019) and use basic statistical methods in an attempt to find the most influential landslide properties for this particular setting. Combined, we present 16 simulations for verification, 16 simulations for validation and 112 simulations for the scaling analysis. All simulations are conducted in a two-dimensional domain (a vertical slice of the tank), although the mathematical model is capable of fully three-dimensional simulations.

The paper is organised as follows: In section 2, we will introduce the multiphase Navier-Stokes Equations as implemented in OpenFOAM and an improved stability criterion for the time step duration that allows us to achieve the required accuracy in tsunami simulations. Further, we introduce dimensionless landslide and tsunami properties and scaling relations from literature. We verify and validate the method in section 3 in terms of the experiments of Bullard et al. (2019). Section 4 extends the parameter space of simulations for a comprehensive sensitivity and scaling analysis, followed by a discussion in section 5. Finally, we give a summary and an outlook in section 6.

2. Methods

2.1. Mathematical model

We apply the unsteady multiphase RANS Equations to simulate a system of multiple fluids (in here water and air), given as

$$\nabla \cdot \mathbf{u} = 0, \tag{1}$$

$$\frac{\partial \rho \, \mathbf{u}}{\partial t} + \nabla \cdot (\rho \, \mathbf{u} \, \mathbf{u}) = - \nabla \, p + \nabla \cdot (2 \, (\mu + \mu_t) \, \mathbf{D}) + \rho \, \mathbf{g}. \tag{2}$$

$$\frac{\partial \alpha_i}{\partial t} + \nabla \cdot (\alpha_i \, \mathbf{u}) + \sum_j \nabla \cdot (\alpha_i \, \alpha_j \, \mathbf{u}_{r,ij}) = 0. \tag{3}$$

Phase indicator functions α_i are defined as

$$\alpha_i(\mathbf{x}, t) = \begin{cases} 1 & \text{phase } i \text{ present at } \mathbf{x}, t, \\ 0 & \text{else,} \end{cases} \tag{4}$$

and allow tracking of the various phases. Numerical diffusion is counteracted by the third term in Eq. (3) using the relative velocity between phases $\mathbf{u}_{r,ij}$, which is constructed to ensure sharp interfaces (Rusche, 2002; Weller, 2008; Marschall et al., 2012). The local fluid density $\rho(\mathbf{x}, t)$ and molecular dynamic viscosity $\mu(\mathbf{x}, t)$ follow from present phases and the respective densities ρ_i and viscosities μ_i,

$$\rho = \sum_i \alpha_i(\mathbf{x}, t) \, \rho_i, \tag{5}$$

$$\mu = \sum_i \alpha_i(\mathbf{x}, t) \, \mu_i. \tag{6}$$

We assume constant fluid densities and viscosities in the following, as this describes water and air reasonably well. All phases advect with the velocity $\mathbf{u}(\mathbf{x}, t)$ and the strain rate tensor $\mathbf{D}$ is defined in terms of its gradient as

$$\mathbf{D} = \frac{1}{2} \left(\nabla \, \mathbf{u} + (\nabla \, \mathbf{u})^T \right). \tag{7}$$

The gravitational acceleration is $\mathbf{g}$ and $p(\mathbf{x}, t)$ is the pressure field. The eddy viscosity $\mu_t(\mathbf{x}, t)$ is supposed to consider effects of turbulence that is not resolved by the numerical discretisation and is calculated with the k-ε-model (Launder and Spalding, 1974) as

$$\mu_t = \rho \, C_\mu \frac{k^2}{\varepsilon}. \tag{8}$$

The turbulent kinetic energy $k(\mathbf{x}, t)$ and rate of dissipation $\varepsilon(\mathbf{x}, t)$
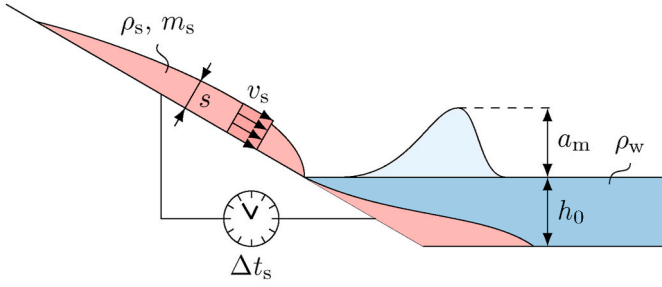
Fig. 1. Landslide (shown in red) and wave (shown in blue) properties. Note that the definition of the averaged velocity and landslide thickness depends on the respective setup and is not generally applicable. (For interpretation of the references to colour in this figure legend, the reader is referred to the Web version of this article.)

follow as

$$\frac{\partial \rho\, k}{\partial t} + \nabla\cdot(\rho\, k\, \mathbf{u}) = $$
$$\nabla\cdot\left(\left(\frac{\mu_t}{\sigma_k} + \mu\right)\nabla k\right) + \mu_t\,(2\,\mathbf{D}):\nabla\,\mathbf{u} - \rho\,\varepsilon, \tag{9}$$

$$\frac{\partial \rho\, \varepsilon}{\partial t} + \nabla\cdot(\rho\, \varepsilon\, \mathbf{u}) = $$
$$\nabla\cdot\left(\left(\frac{\mu_t}{\sigma_\varepsilon} + \mu\right)\nabla \varepsilon\right) + \frac{C_1\,\mu_t\,\varepsilon}{k}\,(2\,\mathbf{D}):\nabla\,\mathbf{u} - C_2\,\rho\,\frac{\varepsilon^2}{k}. \tag{10}$$

Standard parameters, $C_\mu = 0.09$, $\sigma_k = 1.0$, $\sigma_\varepsilon = 1.3$, $C_1 = 1.44$, $C_2 = 1.92$ (Versteeg and Malalasekera, 2007), have been applied in early model tests and the achieved accuracy required no adjustment.

2.2. Numerical solution and stability

The computational domain (in time and space) is discretized to solve the governing equations (1)–(10). The spatial domain is divided into a finite number of polyhedra and the finite volume method (e.g. Weller et al., 1998; Jasak, 1996; Moukalled et al., 2016) is applied to discretize all spatial derivatives. The temporal domain (i.e., the simulation time) is split into a finite number of time steps, and the equations are solved in a time-marching manner. Pressure-velocity coupling is conducted with a semi-implicit method, similar to the PISO algorithm (Issa, 1986) and the governing equations are solved sequentially. Temporal derivatives are discretized with a semi-implicit Euler scheme. The governing equations for phase indicator functions are solved with the MULES algorithm (multi-dimensional limiter for explicit solution, Weller, 2006).

A sequential solution implies that components of the velocity are solved independently and only coupled through explicit terms. This gives rise to stability criteria that limit the time step duration Δt, known as CFL condition (Courant et al., 1928). For convection dominated cases (and uniform grid size Δx), the CFL number is given as

$$\mathrm{CFL}^{\mathrm{conv}} = \frac{|\mathbf{u}|\,\Delta t}{\Delta x}, \tag{11}$$

and has to be limited to a value that is characteristic for the time integration scheme (e.g. 1 for explicit Euler). This is done by choosing the time step duration Δt accordingly. High viscosity in the transient convection diffusion equation (3) leads to a stronger constraint of the time step duration (see appendix A for an in-depth discussion) and the CFL number for such a case is given as

$$\mathrm{CFL}^{\mathrm{diff}} = \frac{\mu\,\Delta t}{\rho\,\Delta x^2}. \tag{12}$$

As we will show in the following, criterion (12) is imperative for convergence, stability and reliability in our applications, which will

often lead to a stricter time step constraint than Eq. (11).

2.3. Dimensionless properties and scaling relations

We compare numerical simulations and physical experiments with several past experiments from literature. The comparison is based on semi-empirical relations for the near field wave amplitude a_m, that are derived from respective experiments. These relations are defined in terms of standardized dimensionless parameters, encoding the average landslide velocity $\bar{v}_s$, the average landslide thickness $\bar{s}$, the landslide width b, the landslide mass m_s, the landslide density ρ_s, the total landslide duration Δt_s, the water reservoir density ρ_w and the water reservoir depth h_0, see Fig. 1. All landslide parameters are averaged over the duration of the impact ($\Delta t_{75\%}$, see section 3.2) in this work, however, some previous works apply the respective peak values (e.g. Heller and Hager, 2010). The derivation of these properties from simulation and experiment is specific to the case setup and thus explained in the respective section.

The dimensionless slide mass is defined as

$$M = \frac{m_s}{\rho_s\, b\, h_0^2}, \tag{13}$$

the dimensionless slide thickness as

$$S = \frac{\bar{s}}{h_0}, \tag{14}$$

and the slide Froude number as

$$\mathrm{F} = \frac{\bar{v}_s}{\sqrt{g\, h_0}}. \tag{15}$$

We note that the slide Froude number in principle defines regions of subcritical ($\mathrm{F} < 1$, wave runs away from the landslide), critical ($\mathrm{F} = 1$), and supercritical ($\mathrm{F} > 1$, wave remains in the generation region) flow. However, as F is based on the terminal water depth h_0, some supercritical flow will always take place near the shoreline. Further, the dimensionless landslide impact duration is defined as

$$\Delta T = \Delta t_s\,\sqrt{\frac{g}{h_0}}, \tag{16}$$

and the relative slide density as the ratio between slide and reservoir densities,

$$R = \frac{\rho_s}{\rho_w}. \tag{17}$$

However, R is unity throughout this work, as $\rho_s = \rho_w$. Furthermore, the cosine of the impact angle α is used in some scaling relations.

The dimensionless near field wave amplitude is defined as

$$A_m = \frac{a_m}{h_0}. \tag{18}$$

Five scaling relations for this important wave parameter,

$$A_{m,SR} = A_{m,SR}(M, \mathrm{F}, S, \Delta T, R, \cos(\alpha)), \tag{19}$$

were experimentally evaluated by Bullard et al. (2019) and the test is repeated here with the numerical results. The first relation is given by Heller and Hager (2010) for granular slides as

$$A_{m,HH10} = \frac{4}{9}\,\mathrm{F}^{4/5}\,S^{2/5}\,M^{1/5}\,\cos\left(\frac{6}{7}\alpha\right)^{2/5}. \tag{20}$$

Zitti et al. (2015) found

$$A_{m,Z15} = \frac{1}{5}\,\mathrm{F}^{1/5}\,S^{3/20}\,M^{9/20}\,\cos(\alpha)^{7/20}, \tag{21}$$

and

Table 1
Parameter ranges of experiments on which the semi-empirical scaling relations are based on.

Parameter	this study	Bullard et al. (2019)	Fritz (2002)	Heller and Hager (2010)	Zitti et al. (2015)
material	liquid	liquid	granular	granular	granular
porosity	0	$\approx 0-0.3$	≈ 0.5	≈ 0.4	≈ 0.5
F	0.041–3.5	2.1–5.4	1.1–4.7	0.86–6.8	0.84–1.9
S	0.017–.4	0.04–0.36	0.076–0.66	0.09–1.6	0.026–0.31
M	0.025–5.3	0.077–6.3	0.12–2.4	0.11–10.0	0.029–0.53
R	1	1	1.7	0.59–1.7	≈ 0.5
A	$10° - 60°$	30°	45°	$30° - 90°$	30°

$$A_{m,Z\Delta t} = \frac{1}{2} \, F^{1/5} \, M^{4/5} \, \Delta T^{-1/5} \, \cos(\alpha)^{7/10}. \tag{22}$$

for buoyant slides, e.g. snow avalanches. Mulligan and Take (2017) derived an approximation based on physical principles,

$$A_{m,q} = \sqrt{1 + R \, S \, F^2 \, \cos(\alpha)^2} - 1, \tag{23}$$

and Bullard et al. (2019) corrected it for high mobility slides to

$$A_{m,q,max} = \sqrt{1 + 2 \, R \, S \, F^2 \, \cos(\alpha)^2} - 1. \tag{24}$$

In addition, we will test the scaling relation of Fritz (2002) for granular landslides, given as

$$A_{m,F02} = \frac{1}{4} \, F^{7/5} \, S^{4/5}. \tag{25}$$

Note that some of these relations address different systems than investigated in here, e.g. granular material ($A_{m,F02}$, $A_{m,HH10}$) and buoyant slides ($A_{m,Z15}$, $A_{m,Z\Delta t}$). Further, definitions for the slide parameters can vary, e.g. by applying averaged or peak landslide parameters. An overview over respective parameter ranges can be found in Table 1. It should not be expected that they are applicable without modification. Therefore, we will systematically evaluate and optimize the respective structures for our conditions in section 4. We also stress that the experimental setups have been different, ranging from gravity driven liquid slides to piston-accelerated granular slides. This has to be taken into account when the scaling relations are compared with the outcome of the present simulations. Furthermore, some of the experiments might be influenced by scaling effects, expected at reservoir depths of $h = 0.2$ m or less (Heller et al., 2008).

3. Validation simulations

3.1. Simulation setup

For the verification of the numerical method and the validation of the mathematical model, we first aim to reproduce the physical experiments of Bullard et al. (2019). The landslide is represented by an elevated water reservoir having a volume V_0. It is released from rest and accelerates due to gravity along the sliding plane inclined with an angle $\alpha = 30°$, finally reaching the water reservoir with a still water depth h_0 (Figs. 2 and 3). We used the solver *multiphaseInterFoam* (v1812) that implements Eqs. (1)-(10) and we extended it to consider the viscous contribution to the CFL criterion (Eq. (12)). We make use of two phases in the simulation, namely water ($\rho_w = 1\,000$ kg m^{-3}, $\mu_w = 10^{-3}$ kg m^{-1} s^{-1}), represented by phase indicator α_w and air ($\rho_a = 1$ kg m^{-3}, $\mu_a = 1.48\cdot10^{-5}$ kg m^{-1} s^{-1}), represented by phase indicator α_a. Note also that different phases for the landslide and the water
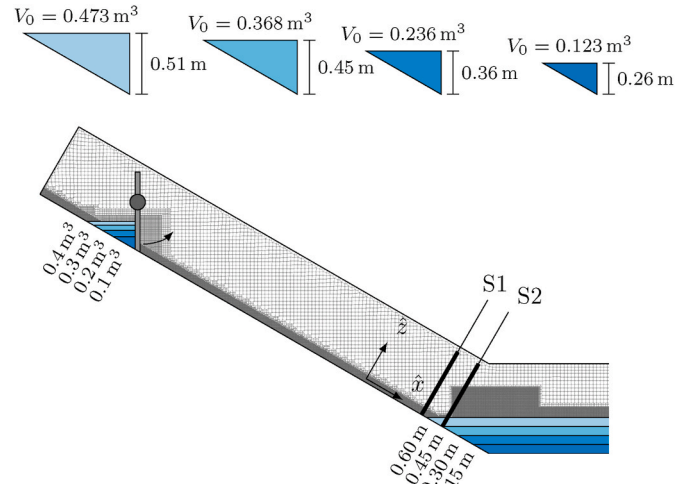
Fig. 3. Close-up of the ramp: the initial volume V_0 and the still water depth h_0 have been varied between 0.1 m^3 and 0.4 m^3 and 0.15 m and 0.60 m, respectively. The coarsest mesh is shown in grey in the background. Slide velocity $v_s(t)$ and thickness $s(t)$ are measured at S1 in the numerical simulations (moved up from S2 where it is measured in experiments).

Table 2
Volumetric discharge, timings of the slide and mean slide properties. The discharged volume V is calculated by integrating the product of slide thickness and slide velocity at the measurement point (S1 or S2).

| Case	discharge	slide dur.	gen. dur.	slide vel.	slide thickness
	V	Δt_s	$\Delta t_{75\%}$	$\bar{v}_s$	$\bar{s}$
Experiment					
$V_0 = 0.123$ m^3	0.122 m^3	0.97 s	0.38 s	5.10 m s^{-1}	0.022 m
$V_0 = 0.236$ m^3	0.223 m^3	1.13 s	0.50 s	5.11 m s^{-1}	0.031 m
$V_0 = 0.368$ m^3	0.360 m^3	1.10 s	0.57 s	5.41 m s^{-1}	0.042 m
$V_0 = 0.473$ m^3	0.627 m^3	1.17 s	0.62 s	6.53 m s^{-1}	0.055 m
Numerics					
$V_0 = 0.123$ m^3	0.118 m^3	1.20 s	0.59 s	5.03 m s^{-1}	0.014 m
$V_0 = 0.236$ m^3	0.227 m^3	1.43 s	0.63 s	5.83 m s^{-1}	0.023 m
$V_0 = 0.368$ m^3	0.356 m^3	1.60 s	0.68 s	6.34 m s^{-1}	0.030 m
$V_0 = 0.473$ m^3	0.460 m^3	1.69 s	0.71 s	6.61 m s^{-1}	0.036 m
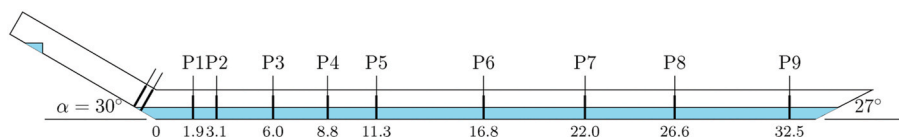
Fig. 2. Overview over the simulation setup following the physical experiments of Bullard et al. (2019). Nine gauges are registering the wave amplitude at P1-9. Distances are shown in meters.
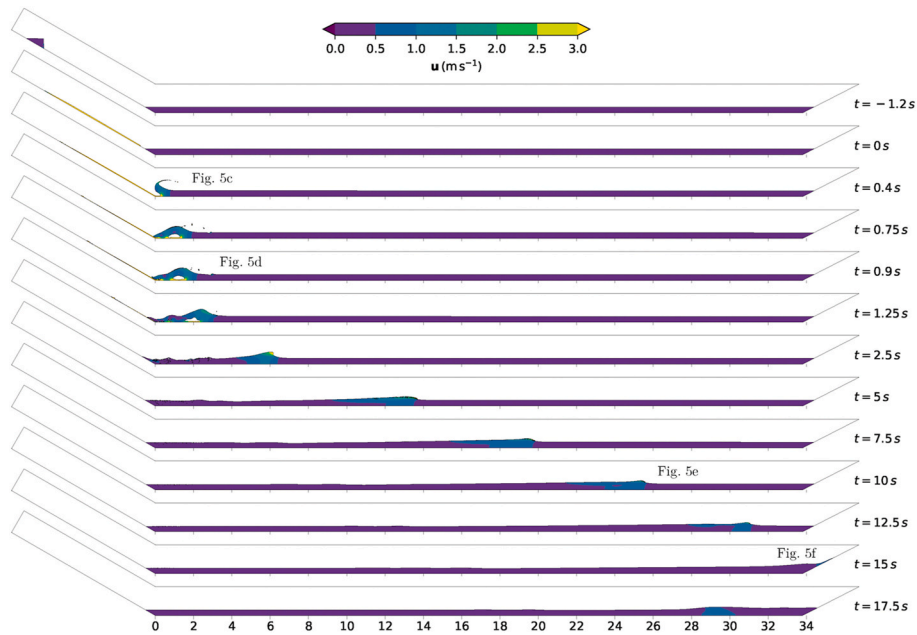
Fig. 4. Time sequence of the simulation with $V_0 = 0.4 \text{ m}^3$, $h_0 = 0.3 \text{ m}$, $\text{CFL}^{\text{diff}} < 1$ and $\Delta x = 0.01 \text{ m}$.
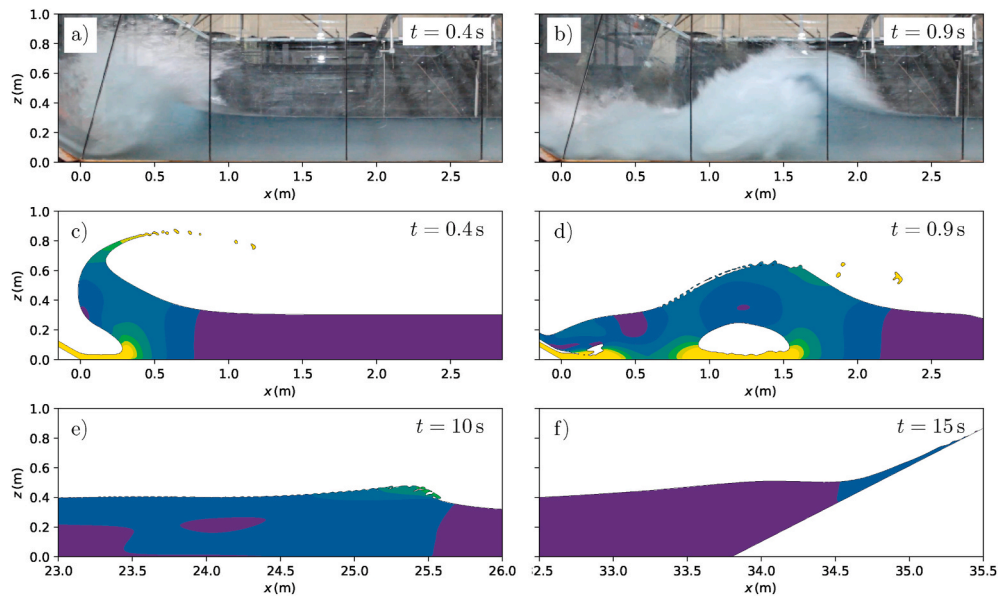

Fig. 5. Stages of the landslide tsunami in detail and in comparison with the experiment: (a, c) The early impact and the plunging wave, (b, d) the formation of a shallow wave, (e) propagation of the wave and (f) inundation and reflection of the wave on the counter slope. Parameter and colour scale as in Fig. 4. (For interpretation of the references to colour in this figure legend, the reader is referred to the Web version of this article.)

reservoir are possible with the applied method, enabling different rheologies and densities in the landslide. However, this was not required for the investigated cases, as the water phase is used to represent both the reservoir water body and the sliding material.

The experiment was conducted in a tank with width $b = 2.1 \text{ m}$. The reservoir that initially holds the landslide is restricted to a width of 1.7 m for constructive reasons related to the release mechanism. We approximate the experimental setup with a two-dimensional numerical setup that corresponds to a tank with constant width b. The reduced width of the landslide reservoir cannot be modelled directly with a two-dimensional setup and we approximate this geometry with a decreased fill height, keeping the landslide volume V_0 constant. The respective volume equivalent fill heights are shown in Fig. 3. The error related to this simplification is expected to be small in comparison to other

modelling uncertainties. All boundaries are modelled as impenetrable walls ($\mathbf{u} = 0$, $\mathbf{n} \cdot \nabla p = 0$, with the boundary normal vector $\mathbf{n}$), except the horizontal top boundary of the tank, which is modelled as a free outlet ($\mathbf{n} \cdot \nabla \mathbf{u} = 0$, $p = 0$, $\mathbf{n} \cdot \nabla \alpha_w = 0$ for outward pointing velocity and $\alpha_w = 0$ for inward pointing velocity). The initial conditions for α_w and α_a are defined by the landslide volume V_0 and the still water depth h_0, the velocity is initially zero. We use four different landslide volumes (roughly $0.1 \text{ m}^3 - 0.4 \text{ m}^3$, see Table 2 and Fig. 3) and four still water depths ($0.15 \text{ m} - 0.60 \text{ m}$, see Fig. 3) leading to overall 16 different cases that have been simulated for validation. Simulations and experimental measurements are synchronised with the arrival time of the landslide at the water basin (i.e. arrival of the landslide front at point S1), which we define as $t = 0 \text{ s}$.
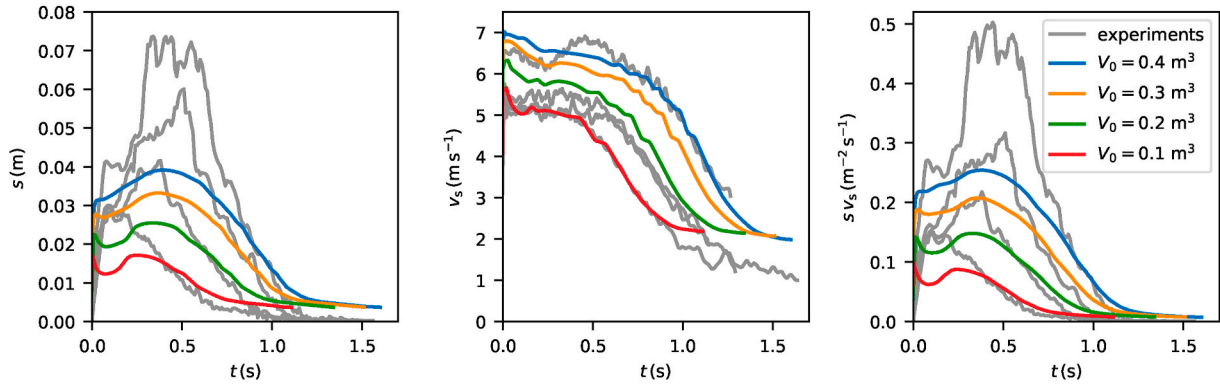
Fig. 6. Simulated slide thickness (coloured lines, left), depth-averaged slide velocity (coloured lines, middle) and landslide momentum (coloured lines, right). For comparison the experimental data is shown in grey. (For interpretation of the references to colour in this figure legend, the reader is referred to the web version of this article.)

The experimental slope and tank geometry is covered by a body fitted mesh with a height of 1.5 m, as shown in Fig. 2. For the exact geometry we refer to Bullard et al. (2019). The mesh was generated using *cartesian2DMesh*, a mesh generator of the cfMesh toolbox (Juretić, 2015). The mesh is dominated by hexagons with aspect ratio one and the faces align with the horizontal water surface. This circumvents numerical artefacts of the free surface at rest. The meshed tank is sufficiently tall to cover the highest waves and to keep enough distance from the boundary to prevent potential influences. Local mesh refinements were applied to the landslide slope, the impact area and the location of the free water surface, reducing the mesh size locally by a factor of four (see Fig. 3). The total simulation duration was set to 20 s which is sufficient to cover the full wave propagation through the tank for most cases, except very shallow ones.

A mesh refinement study (cell sizes and cell numbers in Table 3) was conducted for the case with $h_0 = 0.3$ m and $V_0 = 0.4$ m^3. Additional investigations with other configurations (not shown) provided similar findings. The mesh refinement study was repeated with four different time step durations (defined by CFL criteria, see Table 3), leading to overall 16 simulations that were executed for verification. The time step duration is dynamically adapted following the CFL criterion and its average lies between 10^{-4} s and 10^{-3} s, the smallest time step with $\Delta t \approx 10^{-5}$ s is found in the sliding phase. In the initial simulations we observed severe convergence problems with the conventional (i. e. convective) CFL condition (Eq. (11)), independent of the chosen limit. We found an appropriate time stepping method limited by CFL$^{\text{diff}} < 1.0$ and CFL$^{\text{conv}} < 0.5$ and an appropriate mesh size of 0.01 m that have been used for all simulations if not stated otherwise. This simulation is presented in form of a time sequence in Fig. 4, showing landslide release ($t = -1.2$ s), wave generation ($t = 0 - 1.25$ s), wave propagation ($t = 1.25 - 12.5$ s), inundation ($t = 15$ s) and wave reflection ($t = 17.5$ s). Different stages of the impulse wave are highlighted in Fig. 5. The impact and wave generation is shown in Fig. 5c and 5d alongside a fotograph of the experiment in Fig. 5a and 5b. Notably, a large bubble of air gets trapped by the plunging wave. A similar pattern can be observed in the experiment, however, the air is dispersed by turbulence into small bubbles. The propagating wave is highlighted in Fig. 5d and the inundation in Fig. 5e.

3.2. Derivation of landslide metrics from simulations

All landslide parameters are extracted from the simulation with a line probe at S1, as shown in Figs. 2 and 3. Bullard et al. (2019) used cameras with view centre point S2 to extract the same parameters from experiments. We changed the position from S2 to S1 to simplifying the postprocessing, because the original position was partially submerged in some cases. Differences between position S1 and S2 are small (maximum

difference in velocity ≈ 0.2 m s^{-1}, maximum difference in thickness ≈ 0.003 m) and can be neglected. The slide thickness $s(t)$ is calculated as the highest point at S1 in a slope parallel coordinate system where α_w exceeds 0.5,

$$s(t) = \max\left(\widehat{z}\big|_{\alpha_w(\widehat{z},t)>0.5}\right), \tag{26}$$

with the slope local coordinate $\widehat{\mathbf{x}} = (\widehat{x}, \widehat{z})^T$ as shown in Fig. 3. The depth-averaged slide velocity at S1 is calculated by averaging over the water phase,

$$v_s(t) = \frac{\int_0^\infty \alpha_w(\widehat{z},t) \, |\mathbf{u}(\widehat{z},t)| \, \mathrm{d}\widehat{z}}{\int_0^\infty \alpha_w(\widehat{z},t) \, \mathrm{d}\widehat{z}}. \tag{27}$$

The slide thickness and velocity are presented and compared with the physical experiment in Fig. 6 for all four slide volumes V_0. The mean slide thickness

$$\overline{s} = \frac{1}{\Delta t_{75\%}} \int_0^{\Delta t_{75\%}} s(t) \, \mathrm{d}t \tag{28}$$

and mean slide velocity

$$\overline{v}_s = \frac{1}{\Delta t_{75\%}} \int_0^{\Delta t_{75\%}} v_s(t) \, \mathrm{d}t \tag{29}$$

are calculated as averages over the time period $\Delta t_{75\%}$, which is the time during which 75% of the volume passes the point. The total landslide duration Δt_s is defined as the time period during which the slide height $s(t)$ continuously exceeds 0.0008 m (in accordance with Bullard et al. (2019)). The total mass is calculated as

$$m_s = \int_0^\infty \int_0^\infty b \, \rho_w \, \alpha_w(\widehat{z},t) \, |\mathbf{u}(\widehat{z},t)| \, \mathrm{d}\widehat{z} \, \mathrm{d}t, \tag{30}$$

with the width of the tank $b = 2.10$ m. Timings and averaged properties of the slide are presented and compared with the physical experiment in Table 2.

3.3. Derivation of wave metrics from simulations

The wave properties are measured at nine virtual gauges (i.e. line probes) that are positioned as in the experiments, see Fig. 2. The free surface elevation $\eta_i(t)$ at the i-th wave gauge is calculated as

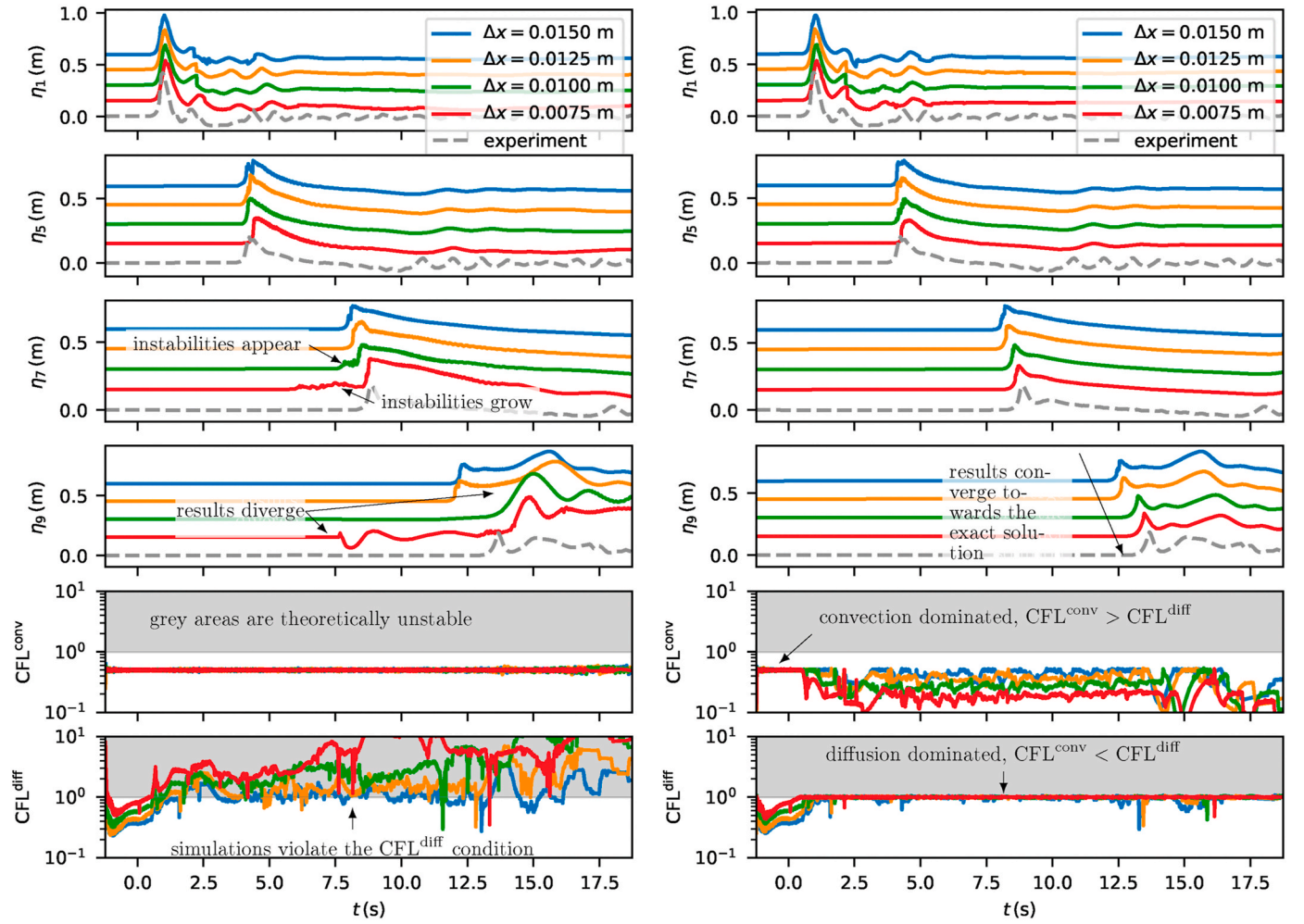$$\eta_i(t) = \max\left(z\big|_{\alpha_w(z,t)>0.5}\right) - h_0. \tag{31}$$

Fig. 7. Wave gauges of experiments with a landslide volume of $V_0 = 0.4$ m³ and water height $h_0 = 0.3$ m. Results of different meshes are shown and offset vertically by 0.15 m for the sake of clearness. Conventional time stepping (left) with $CFL^{conv} < 0.5$ and improved time stepping (right) with $CFL^{conv} < 0.5$ and $CFL^{diff} < 1$. Results with the conventional time stepping criterion are affected by instabilities and diverge from the exact solution with mesh refinement. Results with the improved time stepping are reasonable and converge towards the exact solution for finer meshes. The last two columns show the CFL-numbers. It is clear that unphysical behaviour is related to $CFL^{diff} > 1$ (left). The first wave crest at gauge P9 is also highlighted in Table 3.

Single droplets, which are recognized as short and high peaks in $\eta_i(t)$, are excluded. The resulting free surface elevation time series η_i is shown in Fig. 7 for different cell sizes and time step durations. The full set of results, with all combinations of V_0 and h_0, is shown in appendix B. The first wave crest at gauge i, $a_{m,i}$ is identified as the first local maximum within an interval of 0.4 s that exceeds the minimum value within this interval for 0.04 m. The time that corresponds to the first local maximum is defined as arrival time. The first wave crest is shown as a function of the still water depth for all gauges and all simulations in Fig. 8 to investigate the wave crest limit $a_{m,i} \to 0.6 \, h_0$, that was found by Bullard et al. (2019). The near field wave amplitude as used in scaling relations is defined as the first wave crest at gauge P1 (Bullard et al., 2019), $a_m = a_{m,1}$.

3.4. Verification

We verify the numerical method by ensuring convergence through grid refinement. Considering the early stage of the wave generation, all time stepping criteria perform well. It can be seen in Fig. 7 that the convective CFL criterion is stricter than the diffusive CFL criterion until $t = 0.5$ s. In other words, the flow is convection dominated ($CFL^{diff} < CFL^{conv}$) until the impact because of the fast travelling landslide and the

assumption of the traditional CFL criterion holds. The model behaviour changes drastically during wave propagation which can be seen best at the last gauge P9. The traditional time stepping criterion becomes unstable and the numerical method diverges for finer meshes. The contribution of the viscous term to the CFL number, CFL^{diff}, reaches values 50 times higher than CFL^{conv}. This shows that the momentum transfer is dominated by viscous stresses at the later stages of the simulations. This issue could only be solved with the modified (i.e. diffusive) condition, Eq. (12) and both, the wave crest (Table 3) and the arrival time converge towards the exact solution. Further, we found with this analysis that results show a numerical uncertainty (Roache, 1997) of a few percent at a mesh resolution of $\Delta x = 0.01$ m. This mesh size was hence used in all simulations. The case with $\Delta x = 0.01$ m, $h_0 = 0.3$ m and $V_0 = 0.4$ m³ requires an execution time of roughly 24 h on 20 cores of an Intel Xeon E5-2690 v4 CPU. The same simulation with $\Delta x = 0.0075$ m takes roughly 70 h, while changes in h_0 and V_0 have little influence on the execution time. This shows that further refinement is problematic due to the inverse quadratic scaling of CFL^{diff} with the cell size Δx.
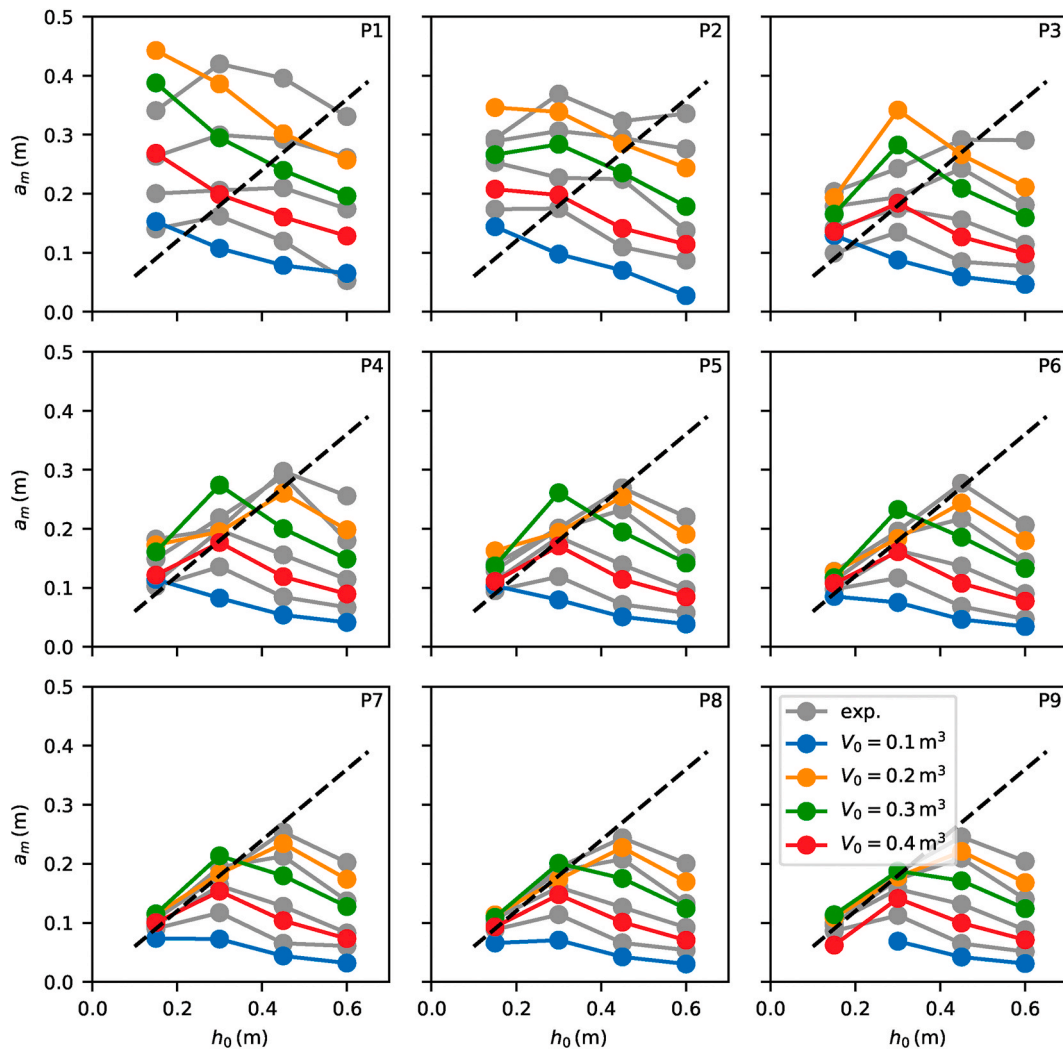
Fig. 8. The first wave crest at Gauges P1-9 for all 16 simulations as a function of the still water depth h_0. The colour marks the landslide volume. Coloured lines represent simulations, grey lines the respective experiments by Bullard et al. (2019). The black dashed line marks the found limit of $a_m \to 0.6\,h_0$. (For interpretation of the references to colour in this figure legend, the reader is referred to the Web version of this article.)

Table 3
Difference in first wave crest at Gauge P9 between experiment and simulation for various meshes and time step settings.

	$\Delta x = 0.015$ m	$\Delta x = 0.0125$ m	$\Delta x = 0.01$ m	$\Delta x = 0.0075$ m
	$N = 0.48$ M	$N = 0.69$ M	$N = 1.08$ M	$N = 1.88$ M
$CFL^{conv} < 0.5$	0.027 m (14%)	0.014 m (8%)	0.196 m (105%)	0.150 m (81%)
$CFL^{conv} < 0.1$	0.020 m (11%)	0.014 m (7%)	0.020 m (11%)	0.038 m (20%)
$CFL^{conv} < 0.05$	0.031 m (16%)	0.009 m (5%)	0.025 m (14%)	0.051 m (28%)
$CFL^{diff} < 1.0$	0.025 m (13%)	0.014 m (8%)	0.001 m (1%)	0.001 m (1%)

Table 4
Errors at selected gauges for the converged ($\Delta x = 0.01$ m, $CFL^{diff} < 1.0$) simulation with $V_0 = 0.4$ m³, $h_0 = 0.3$ m.

before breaking:	P1	P3
$\Delta a_{m,i}$	0.032 m (8%)	0.088 m (36%)
$\Delta t_{m,i}$	0.13 s (14%)	0.26 s (12%)
after breaking:	P5	P9
$\Delta a_{m,i}$	0.013 m (6%)	0.001 m (1%)
$\Delta t_{m,i}$	0.14 s (3%)	0.37 s (3%)

3.5. Validation

3.5.1. Landslide

The slide, represented in terms of the landslide thickness $s(t)$ and landslide velocity $v_s(t)$ at S1 is compared with the physical experiment (at S2) in Fig. 6. The landslide velocity v_s matches the experiment fairly well. Interestingly, the smallest landslide ($V_0 = 0.1$ m³) and the largest landslide ($V_0 = 0.4$ m³) fit best, with differences in mean velocity of less then 0.1 m s^{-1} (1%). On the other hand, the two mid-sized landslides display mean velocity differences up to 0.83 m s^{-1} (15%), as the velocity in simulations increases steadily with landslide volume while
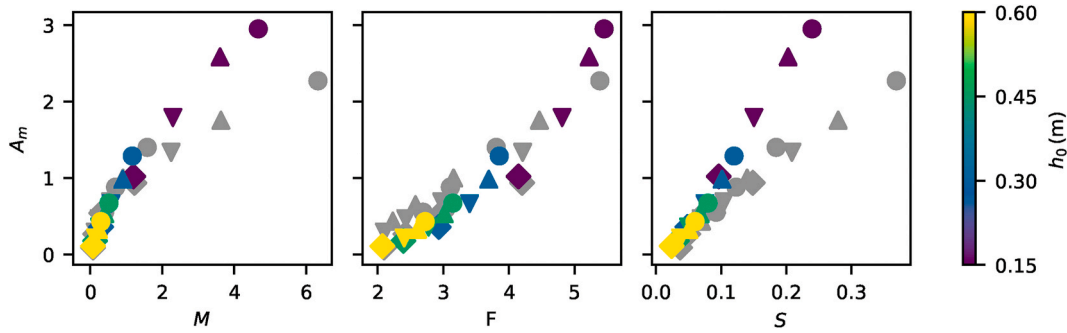
Fig. 9. Dimensionless mean properties of the landslides, the dimensionless landslide mass M, the landslide Froude number F and the dimensionless landslide thickness S, plotted against the dimensionless wave amplitude A_m. The grey marks represent experimental results of Bullard et al. (2019), the coloured marks represent numerical results, coloured after the water depth h_0, marks indicate the landslide volume V_0. (For interpretation of the references to colour in this figure legend, the reader is referred to the web version of this article.)

experiments show a jump between $0.3\,\mathrm{m}^3$ and $0.4\,\mathrm{m}^3$. The landslide velocity is close to the free fall velocity that follows from this drop height ($v_{\max} = 7.5\,\mathrm{m\,s}^{-1}$) and it is safe to assume that basal friction played a minor role in these experiments. The landslide thickness s differs more strongly in all cases. The maximum slide thickness is underestimated by the numerical method, especially for the largest landslide, where a difference in mean slide thickness of 35% can be observed (the difference in the peak is higher). The tail is stretched out and is thicker in the simulations, compensating the reduced volume flux in the front of the landslide, leading to an overall similar volume in experiments and simulations (see Table 2). Only the largest landslide differs substantially from this observation and the experiment shows an apparent discharge of $0.627\,\mathrm{m}^3$ that exceeds the initial landslide volume ($0.473\,\mathrm{m}^3$) by 33%. It should be noted that the thickness of the tail is below the cell size of $\Delta x \approx 0.01\,\mathrm{m}$ and that the numerical model cannot resolve such small length scales. The smallest resolvable length scale can be identified in Fig. 6a as 0.005 m which roughly corresponds to half of the cell size.

3.5.2. Wave

The simulated wave is compared to the experiment in terms of the first wave crest and the arrival time. A direct comparison of the wave gauge data ($\eta_i(t)$) is not practical, as a small error in arrival time can lead to a large apparent error. The respective difference is shown in Table 4 for selected wave gauges of the case $V_0 = 0.4\,\mathrm{m}^3$, $h_0 = 0.3\,\mathrm{m}$ and lies between 1% and 36%, depending on the position of the gauge. The difference is larger in the near field and reaches its peak in the region where the wave is likely breaking while it reduces substantially in the far field. The wave crest amplitude is shown for all configurations and all gauges in Fig. 8 with similar differences. Furthermore this figure highlights the breaking of waves, which eventually leads to a wave amplitude limit of $a_{m,i} \to 0.6\,h_0$ in physical experiments and numerical simulations. The trailing waves that are present in experimental results, especially in the case $V_0 = 0.1\,\mathrm{m}^3$, $h_0 = 0.6\,\mathrm{m}$, can also be found in the numerical simulations (see Fig. 16), however they are substantially lower. Finally, the wave is reflected by the slope at the far end of the flume and the simulation is able to describe this process reasonably well in most cases.

3.6. Scaling relations

The range of dimensionless properties from simulations and experiments is shown in Fig. 9, alongside the dimensionless near field wave amplitudes. Scaling relations are compared to the wave crest as extracted from simulations and from physical experiments in Fig. 10. Moreover, it shows the relative difference, defined as

$$\delta_{\mathrm{SR}} = \frac{A_{m,\mathrm{SR}} - A_m}{A_m}, \tag{32}$$

with $A_{m,\mathrm{SR}}$ being predicted with one of Eqs. (20)-(25) and A_m the corresponding numerical or experimental result. Note that input data for the semi-empirical relation $A_{m,\mathrm{SR}}$ was chosen in correspondence to A_m, either from the experiment or the numerical simulation. Further, it should be noted that a positive difference indicates that the semi-empirical relation overestimates the wave amplitude.

The best fitting relation in terms of experimental results is given by $A_{m,q,\max}$ (Eq. (24)) with an average relative difference of 25%, while the largest difference was given by A_{Z15} (Eq. (21)) with 79%. The same was observed with respect to numerical results with average relative differences of 29% and 79%, respectively. This had to be expected as $A_{m,q,\max}$ was developed for these high mobility flows while A_{Z15} aims to describe buoyant landslides. Interestingly, the relative difference of A_{F02} (Eq. (25)) collapses to a single line, indicating a good fit but a mismatch of a constant factor. These preliminary results on scaling relations are valuable and interesting but show several problems, such as the narrow parameter space and the high correlation between the different landslide parameters. Furthermore, scaling relations have not been adjusted to the characteristics of the presented cases. The extended scaling and sensitivity analysis below aims to resolve some of these problems.

4. Sensitivity and scaling analysis

The concept of a gravity driven, naturally developing landslide is not very convenient for a well defined sensitivity analysis of slide parameters S, F, M, ΔT and basin parameters h_0 and α. Parameters cannot be explicitly controlled and we have to rely on initial conditions to manipulate landslide parameters. Moreover, parameters are widely correlated in such a case (see Fig. 9). In this section, the gravity driven landslide as used in section 3 is therefore replaced with a well controlled boundary condition near to the point of impact as shown in Fig. 11. Natural events span over a wide range of parameters, from slow cliff collapses to fast slides that accelerated on long slopes and we aim to cover this wide range with the modified simulation setup. This concept is similar to the experiments of Fritz (2002), however, with water instead of granules as slide material. With this concept we can lock the slide thickness $s(t) = \bar{s}$, the slide velocity $v_s(t) = \bar{v}_s$ and the landslide duration Δt_s to predefined values. The landslide mass

$$m_s = \rho_s\, b\, \bar{s}\, \bar{v}_s\, \Delta t_s \tag{33}$$

is correlated to these parameters and the landslide density ρ_s. Geometrical properties such as the slope angle α and the still water depth h_0 can be set during geometry generation and simulation initialisation. Note that a variation of the geometry leads to different impact positions (i.e. the point where landslide and reservoir touch first, see Fig. 11) in relation to the position of the first gauge. However, we estimate that the influence of this variation on the wave generation is small, considering
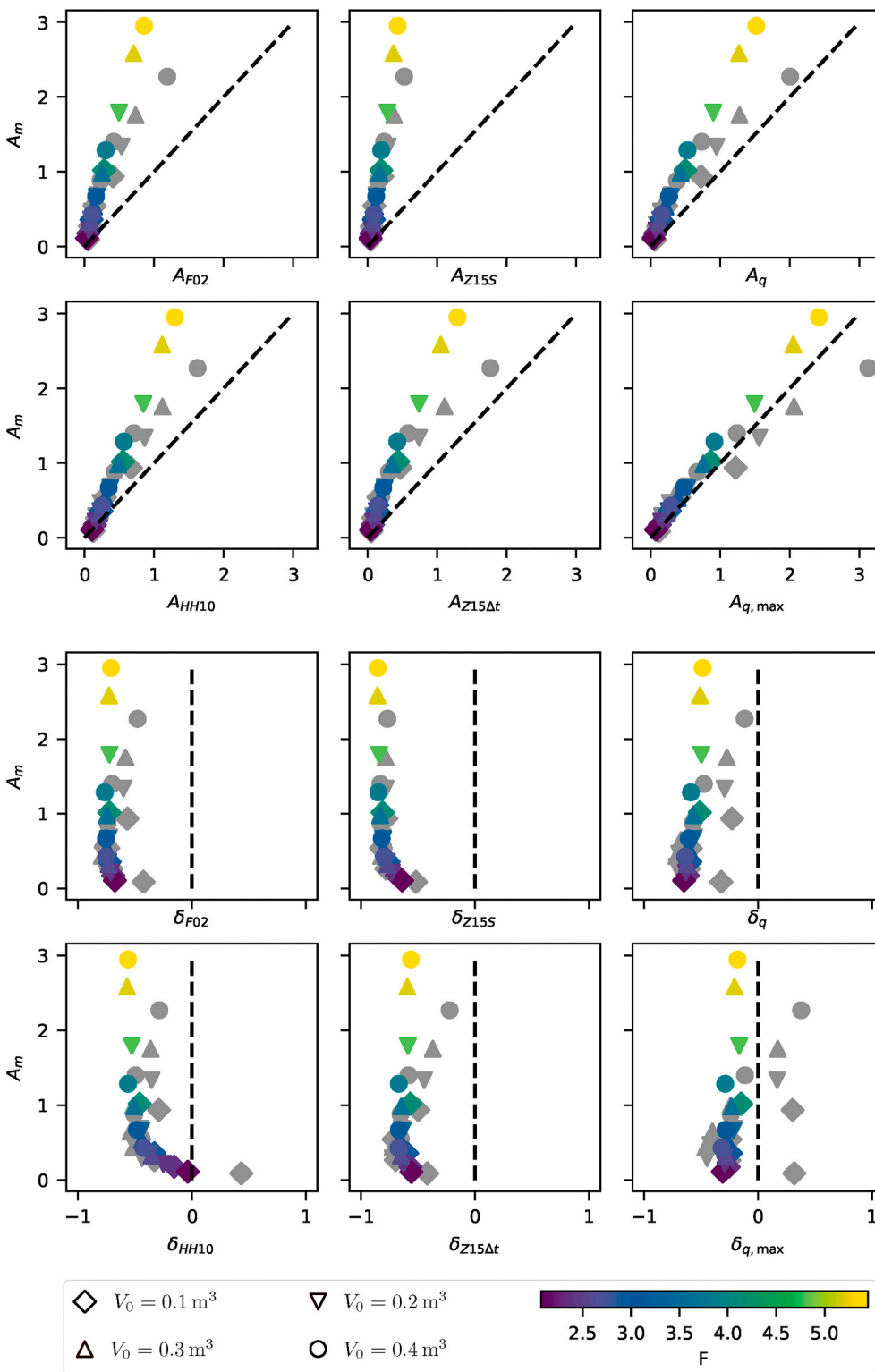
Fig. 10. Semi-empirical models for the first wave crest, A_{F02}, A_{HH10}, A_{Z15S}, $A_{Z15\Delta t}$, A_q and A_{qmax} compared to the measured first wave crest in experiments (grey marks) and the numerical results (coloured marks). The respective differences are shown below. The colour represents the slide Froude number F and the mark represents the landslide volume V_0. The black dashed line indicates a perfect fit. (For interpretation of the references to colour in this figure legend, the reader is referred to the Web version of this article.)

the small change of the wave amplitude between P1 and P2 in the verification cases. Another benefit of the modified case setup is the reduced computation time as the landslide slope and the time before slide impact are not simulated. Moreover, simulation duration and tank extension are reduced to 10 m and 5 s, respectively, and we focus on the first wave gauge P1.

We choose parameters as presented in Tab. 5 to extend the coverage of the parameter space in comparison to section 3. In particular, we are interested in lower Froude numbers to investigate the regime change between subcritical (F < 1) and supercritical (F > 1) wave generation. To reduce the number of required simulations, only selected parameters (underlined in Table 5) are combined with all other parameters. This way, we reduce the number of simulations to 112, without influencing the parameter resolution significantly. Each parameter is applied in at least four simulations. All simulations with the simplified case setup have been executed on a high performance cluster within 24 h, using
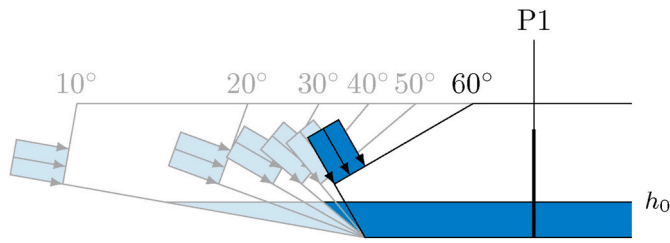
Fig. 11. Modified simulation setup for the sensitivity analysis. Six geometries for six impact angles are shown. The inlet boundary condition, indicated by the arrows, prescribes the velocity $\bar{u}$ over the slide thickness $\bar{s}$ for a duration of Δt. The wave is recorded as before at P1. The geometry is automatically generated and the position of the inlet follows from the still water depth h_0.

Table 5
Slide parameters in the sensitivity analysis. Underlined parameters are combined with all other parameters, non-underlined parameters are combined only with underlined parameters.

slide duration Δt_s	slide velocity $\bar{v}_s$	slide thickness $\bar{s}$	angle α	depth h_0
0.25 s	1 m s^{-1}	0.01 m	10°	0.15 m
0.50 s	2 m s^{-1}	0.02 m	20°	0.30 m
1.00 s	3 m s^{-1}	0.04 m	30°	0.45 m
1.50 s	4 m s^{-1}	0.06 m	40°	0.60 m
	6 m s^{-1}	0.08 m	50°	0.75 m
			60°	0.90 m

about 400 Intel Xeon E5-2690 v4 cores.

The relationship between the simulated dimensionless slide parameters and the first wave crest is presented in Fig. 12. It can be seen that we achieve a wide range of slide parameters and that they are not as correlated as before. The results of the scaling relations and the respective differences are presented in Fig. 13 (see also Table 6). The best fitting relation for this setup is $A_{15\Delta t}$ with an average relative difference of 23%, followed by A_{HH10} with a relative difference of 27%. As before, the difference of relation A_{F02} (Eq. (25)) collapses to a line and the respective difference is similar with roughly 70%. This fact is very interesting and hints towards a strong predictive power of this relation.

A simple statistical analysis gives a good overview over the significant correlations between landslide parameters and the wave amplitude. The correlation between wave amplitude and landslide parameters is given in terms of correlation coefficients as $R(M,A_m) = 0.88$, $R(F,A_m) = 0.74$, $R(S,A_m) = 0.78$, and $R(\Delta T,A_m) = 0.32$. The correlation between the wave amplitude A_m and the slope angle α is very low, $R(\cos(\alpha),A_m) = 0.06$.

Further, a multiple regression was conducted to derive multiple scaling relations with increasing numbers of parameters. Inspired by the high single parameter correlation of landslide mass M with wave amplitude A_m, we first tested a scaling relation solely based on this parameter. The two free parameters were optimized to fit the numerical results, leading to

$$A_{M,1} = 0.45\,M^{0.83}. \tag{34}$$

The wave amplitude is predicted by this relation with an average relative error of 26% and the correlation (R-value) between the relation
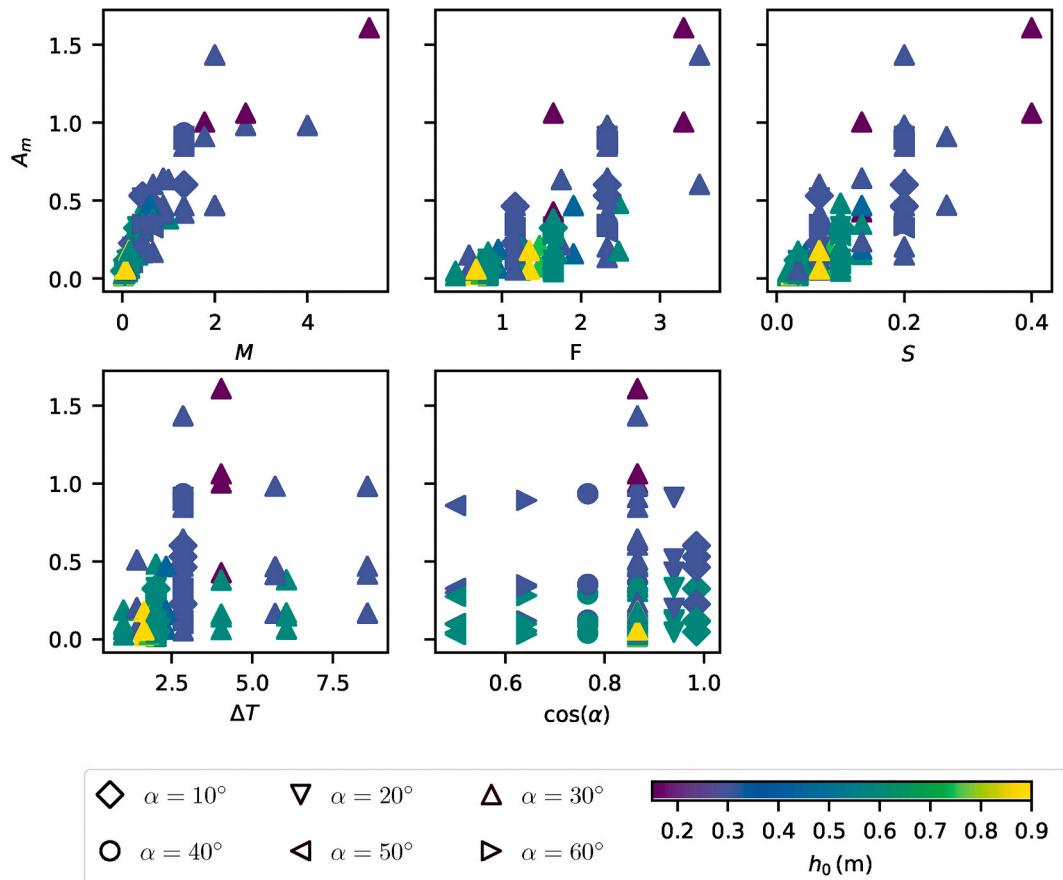

Fig. 12. Dimensionless mean properties of the landslides in the modified and extended simulation setup. The dimensionless landslide mass M, the landslide Froude number F, the dimensionless landslide thickness S, the dimensionless landslide duration ΔT and the cosine of the impact angle $\cos(\alpha)$ are plotted against the dimensionless wave amplitude A_m. The colour represents the still water depth h_0, the mark represents the impact angle α. (For interpretation of the references to colour in this figure legend, the reader is referred to the Web version of this article.)
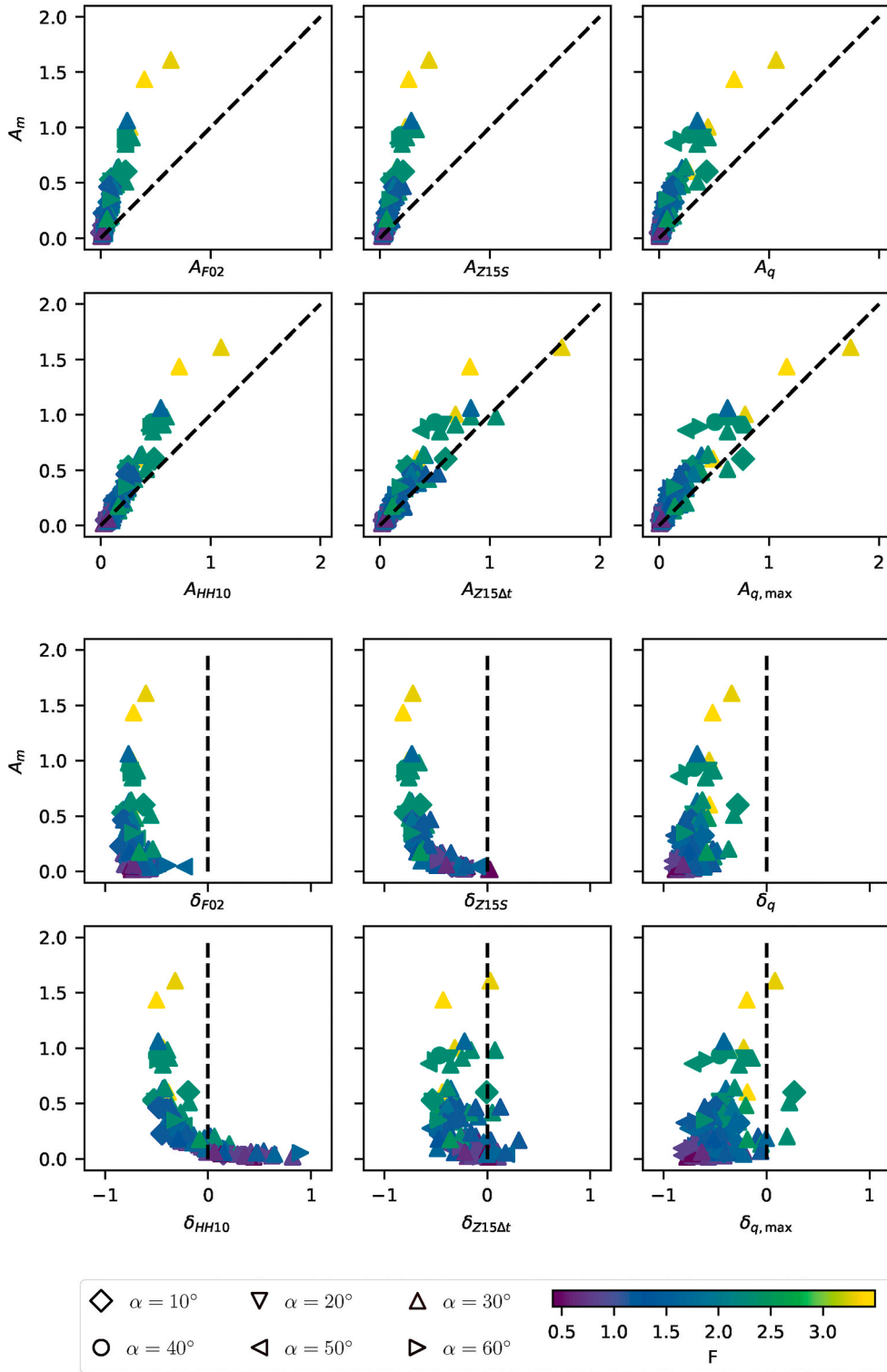
Fig. 13. Semi-empirical models for the first wave crest A_{HH10}, A_{Z15S}, $A_{Z15\Delta t}$, A_q, A_{qmax} and A_{F02} compared the numerical results. The respective differences to simulations are shown below. The colour represents the slide Froude number F, the mark represents the impact angle α. The black dashed line indicates a perfect fit. (For interpretation of the references to colour in this figure legend, the reader is referred to the Web version of this article.)

and simulation is 0.91. A second scaling relation (two parameter relation), inspired by Fritz (2002), is based on Froude number F and slide thickness S,

$$A_{M,2} = 1.3\, F^{1.25}\, S^{0.97} \tag{35}$$

and yields an average relative difference of 20%. The correlation be-

tween predicted and simulated amplitude is 0.95. Powers of F and S are very similar to values reported by Fritz (2002) but the constant factor is about 5 times higher. This was already indicated by Fig. 13, where the difference of relation (25) was appearing as a line. Other relations based on two parameters show a similar performance, e.g.,

$$A_{M,2.2} = 1.0\, M^{0.99}\, \Delta T^{-0.58}, \tag{36}$$

Table 6

Average difference between scaling relations when compared to experiments and numerical simulations. The first block shows relations form literature, the second block shows relations optimized to the inlet driven simulations. They are compared to experiment and the gravity driven simulations (grey numbers) without further optimization.

	Scaling rel.	optimized for	Experiment	gravity driven	inlet driven
literature	A_{F02}	granular slides	68%	73%	71%
	A_{HH10}	granular slides	43%	40%	29%
	A_{Z15S}	buoyant slides	79%	79%	55%
	A_{Z15DT}	buoyant slides	59%	62%	25%
	A_q	granular slides	50%	58%	72%
	$A_{q,max}$	liquid slides	29%	25%	47%
optimized	$A_{M,1}$	simulations	55%	52%	26%
	$A_{M,2}$	simulations	24%	15%	20%
	$A_{M,2.2}$	simulations	72%	64%	18%
	$A_{M,3}$	simulations	31%	20%	16%
	$A_{M,4}$	simulations	26%	16%	14%

based on landslide mass M and landslide duration ΔT (average difference 18% and R-value 0.94). Taking into consideration three parameters,

$$A_{M,3} = 0.83\,F^{0.76}\,S^{0.52}\,M^{0.40}, \tag{37}$$

reduces the average relative difference to 16% (R-value 0.95). Adding the impact angle α (four parameters),

$$A_{M,4} = 0.89\,F^{0.80}\,S^{0.50}\,M^{0.38}\cos(\alpha)^{0.57}, \tag{38}$$

improves results slightly (difference 14%, R-value 0.95). Note that with the present setup, all these parameters and the dimensionless landslide duration ΔT are related through (see also Eq. (33))

$$M = S\,F\,\Delta T \tag{39}$$

and they can be exchanged respectively in Eqs. (37) and (38). Three selected scaling relations ($A_{M,1}$, $A_{M,2}$, $A_{M,3}$) are compared with simulation results in Fig. 14 alongside the relative difference.

Notably, not all relations perform similar if they are applied to the cases of Bullard et al. (2019). As shown in Table 6, especially relations involving the total landslide mass M perform poorly. $A_{M,2}$, based on A_{F02}, performs best in such a scenario.

5. Discussion

5.1. Verification

We observed severe problems with the convective CFL condition (Eq. (11)). A reduction of the limit on CFL^{conv} (as done from 0.5 to 0.1 and further to 0.05) helps to some regard, however, a reliable convergence can only be achieved with the full CFL criterion, including the viscous contributions CFL^{diff}. This can be traced back to the fact that the momentum conservation equation is dominated by viscous stresses. The
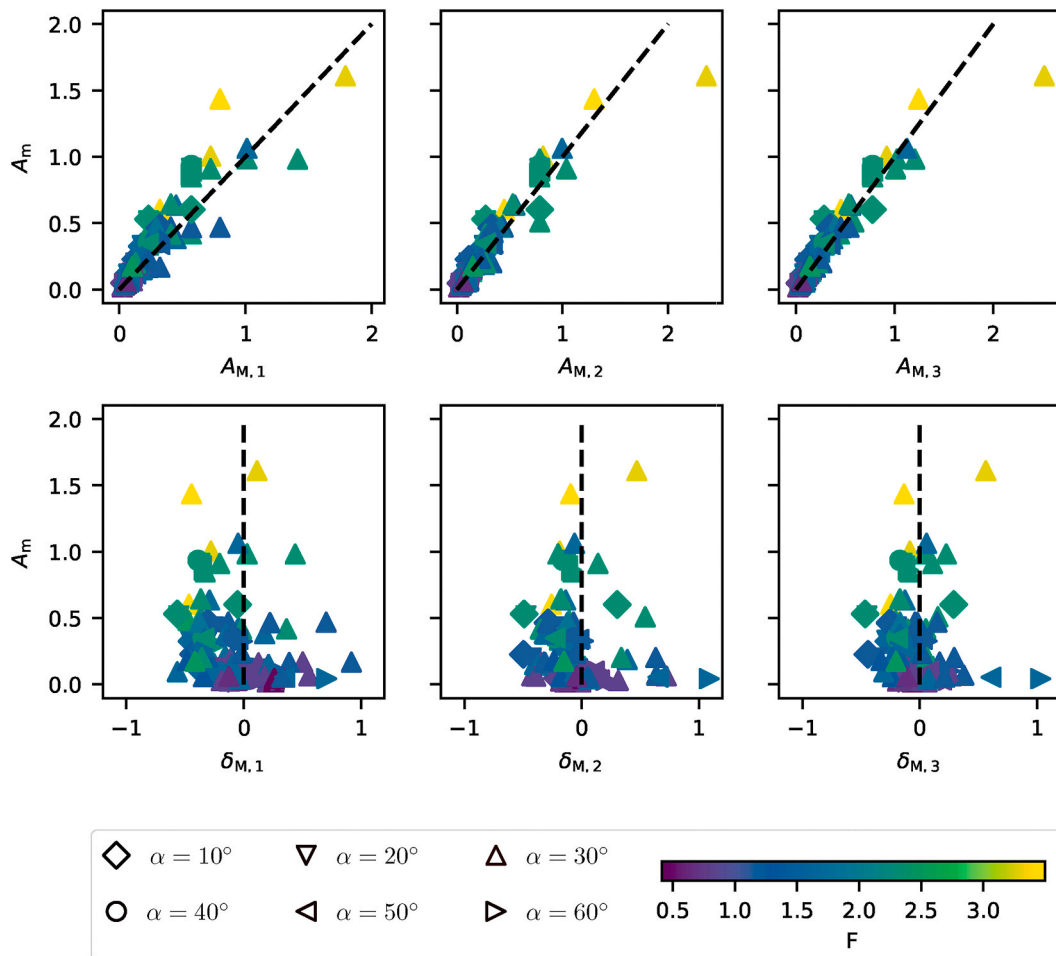

Fig. 14. Optimized relations for the first wave crest with (left to right) 1 parameter ($A_{M,1}$), 2 parameters ($A_{M,2}$) and 3 parameters ($A_{M,3}$) compared to the numerical results. The respective differences are shown below. The colour represents the slide Froude number F and the mark represents the impact angle α. The black dashed line indicates a perfect fit. (For interpretation of the references to colour in this figure legend, the reader is referred to the Web version of this article.)

diffusive term of the partial differential equation has to be taken into account in stability considerations, as already shown by Courant et al. (1928) (see also Ferziger and Perić, 2002; Moukalled et al., 2016, for a more specific interpretation in terms of Navier-Stokes Equations). The domination of viscous stresses can have many reasons, in our cases it can be related to the small scale of the experiment and the respectively small cell size (compare scaling of Eq. (11) with Eq. (12)) while the viscosity itself is not exceptionally high. Furthermore, the jump of the viscosity at the free surface might be problematic.

Most numerical results converge well with the correct time stepping criterion and we estimated a numerical uncertainty of a few percent. Some gauges (P2 to P5) differ from this trend, but these deviations can likely be linked to wave breaking. This issue could probably be addressed by fine-tuning the parameters of the turbulence model, but investigating this is beyond the scope of this paper.

Generally, as reported by Roenby et al. (2017), 10 to 20 cells along the wave crest are required in OpenFOAM with MULES for accurate results of non-breaking waves. This was confirmed by our results which also contain breaking waves. The applied mesh size of $\Delta x = 0.01$ m was sufficient for most waves, although small waves with $a_m < 0.1$ m appear too diffusive in simulations (find the full set of simulations in appendix B). This is especially the case for the trailing wave train following the first wave crest. This confirms once more that at least 10 cells along the wave crest should be used in OpenFOAM. Results appear very accurate with 20 cells along the wave crest and we expect no further improvement with finer meshes as results converge rapidly towards the exact solution. Moreover, further refinement is very expensive for a long tank as used in here, as the numerical cost grows quickly (with $1/\Delta x^4$) due to the strict stability criterion. It should be noted that this issue might not be equally severe for real scale cases. The length scale will be substantially bigger in real scale cases while the viscosity will be similar (depending on landslide rheology). This scaling behaviour will allow comparably large time steps and lower execution times for larger cases.

5.2. Validation

Aside from numerical accuracy, the applied mathematical model was tested for physical accuracy, i.e. if it is appropriate for the considered problem. This is achieved by a comparison of the slide thickness, the slide velocity, the first wave crest amplitude and the arrival time of the wave in simulations and experiments. We want to stress that it is important to only use converged results with low numerical uncertainty in such a comparison.

The simulated landslide velocity fits reasonably well to experiments with two outliers ($V_0 = 0.2$ m^3 and $V_0 = 0.3$ m^3). The reason for this discrepancy could not be conclusively explained. However, we assume that the difference remains within the uncertainty of the experiments and we found the numerical results to be reasonable. The error in the slide thickness is substantially higher. The numerical method is not able to resolve the thin tale of the landslide and it appears with a thickness of 0.005 m in simulations (see Fig. 6). An unrealistic amount of fluid is accumulated in the tail. This volume is missing in the front and middle region of the slide where the thickness is respectively underestimated. Finally, a droplet forms from all the fluid that was left on the slope and that could not be resolved by the numerical method.

This behaviour was observed with all mesh sizes during verification. This might indicate that a substantially finer mesh is required or that the method is not suitable to resolve the thin tale of the fluid landslide. Depth-integrated flow models are not affected by such problems and will perform better in this situation. This issue does not affect the inlet driven simulations for the scaling analysis as the landslide entered the simulation domain close to the impact area with constant and resolvable thickness. The relative error in the maximum slide thickness is roughly 30% for the three small landslides but almost 50% for the largest

landslide. The higher error for the largest slide is related to the increased discharge in the experiment (133% of initial landslide volume). The additional volume in the experimental landslide can probably be traced back to entrainment of air into the turbulent slide which is not represented by the numerical model.

Notably, the boundary layer of the slope has not been resolved either. This layer is of high importance for the basal friction and thus the velocity of the landslide. However, basal friction seems not important in the investigated setup and the velocity is not affected by this issue. This might change for other materials such as granular slides, where the friction is substantially higher and depending on a well resolved boundary layer.

The simulated wave amplitude and the arrival time compare generally well to the experiment. We observe that the error diminishes in the far field. This indicates that the turbulent generation stage and wave breaking is the most challenging problem, while wave propagation and the prediction of the limit $a_{m,i} \rightarrow 0.6\,h_0$ is remarkably accurate. Note, that the limit found in experiments and numerical simulations is considerably lower than the breaking limit for solitary waves close to 0.8 times the water depth.

The highest relative error in the verification case appears at P3 (36%). This difference is likely related to the breaking of the wave, which takes place before P3 in the experiment but after P4 in the numerical simulation. Accordingly, the error at P5 is small (6%) and the far field error at the last gauge, P9, is even smaller (1%). In fact, breaking of waves and the amplitude thereafter is predicted well by the numerical method, compare Fig. 8. However, the timing is very sensitive to diffusive processes in the flow and the exact onset is hence hard to predict with the numerical method. This leads to large errors and partially diverting results at Gauges P2 to P5.

Extending the validation to cases beyond the verification case $V_0 = 0.4$ m^3, $h_0 = 0.3$ m, we found that experimental and numerical near field amplitudes match generally well, with only a few cases giving larger errors (above 25%). The same is the case for far field amplitudes, however, where the error increases for lower wave amplitudes and thus lower landslides volumes to $\Delta a_{m,9} = 0.014$ m for $V_0 = 0.3$ m^3 and $\Delta a_{m,9} = 0.016$ m for $V_0 = 0.2$ m^3. This most likely corresponds to the numerical uncertainty, which is related to the number of cells across the wave crest.

5.3. Scaling relations

The six semi-empirical scaling relations have been compared to the experimental measurements of Bullard et al. (2019) and the respective numerical results in Fig. 10 and Table 6. Further, we extended the parameter space substantially with a simplified setup. In particular, we aimed to cover the more subcritical wave generation indicated by F < 1, different impact angles and higher reservoir depths. The simple statistical analysis showed that the total landslide mass M is the most reliable and most influential landslide parameter for this setting. Moreover, F and S are second most important when used as single correlation parameters. According to our simulations, the impact angle α plays no relevant role for the wave amplitude. However, it should be noted that these results are limited to almost frictionless landslides with density ratio $R = 1$ and that the impact angle might play a role in buoyant or granular slides.

The multiple regression gives us further insight into the wave generation mechanism. The scaling relation with landslide mass M yields an average relative error of 25% in relation to the simulations. Taking into account the velocity of the landslide at impact can reduce the average relative error to 17%. Both of these relations perform exceptionally good considering their simple structure and the wide range of parameters. In fact, the scaling with F and S ($A_{M,2}$, Eq. (35)) yields consistently good results in all simulations as well as in experiments of Bullard et al. (2019) and Fritz (2002). The difference found in the constant factor of this
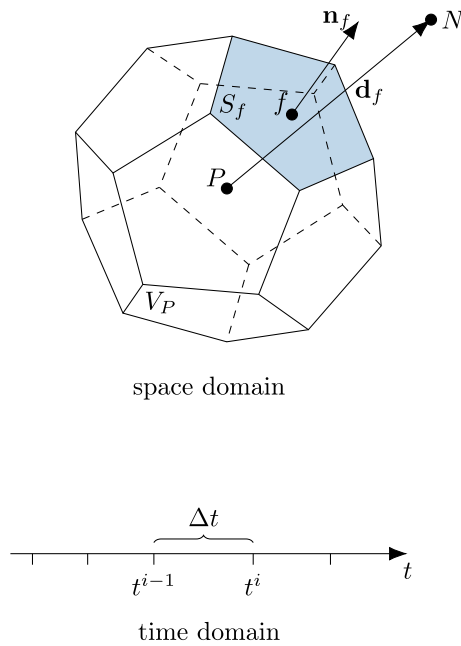
Fig. 15. Discretisation of space is conducted with finite volume cells, (redrawn after Jasak, 1996), the time is split into a finite number of time steps.

relation might be related to the relative density R and a respective extension might further improve the predictive skills of this relation.

$A_{M,1}$ (Eq. (34)) and $A_{M,2.2}$ (Eq. (36)) including the landslide mass M describe the inlet driven simulations well but the predictions can not be transferred to the setup of Bullard et al. (2019), where they perform poorly. We conclude that the landslide mass is transferred into wave energy more efficiently in the inlet driven simulations. This is most likely related to the shape of the landslide and the low energy tail of the naturally evolving landslide which does not contribute to tsunami genesis. The shape of the landslide might be an important factor in real case landslide tsunamis and different failure mechanisms (e.g. cliff collapses with short travel distances (Viroulet et al., 2013)) might require different scaling relations and parameterisations. Relation (35), based on F and S, is not affected by these issues as F and S are estimated from the highly energetic front and middle part of the landslide that actually contribute to tsunami genesis (compare tsunami generation duration $\Delta t_{75\%}$). This shows the limits of scaling relations and that they cannot be transferred to different situations without substantial uncertainties. Properties of the landslide that are not described by mean parameters can have a significant impact on the wave generation and scaling relations are not able to cover these influences. This also highlights the added value of numerical simulations which are able to describe various situations with a single set of parameters.

Interestingly, the simulations allow an estimation of the tsunami generation duration. Fig. 12 shows that the wave amplitude remains constant after the landslide duration reaches a value of approximately $\Delta T = 4$. Further simulations with landslide durations up to $\Delta T = 15$ (not shown) confirmed this conjecture and we estimate the tsunami generation duration to be not longer than

$$\Delta t_{\text{gen,max}} \approx 4 \sqrt{\frac{h_0}{g}}. \tag{40}$$

The landslide mass impacting the reservoir within this duration can be transferred into the tsunami while the remaining mass has no first order effect on the near field wave amplitude.

In the setting investigated here, the basin and especially the impact area are very shallow, which means that the landslide is displacing the water mass horizontally during the impact, mimicking a collisional
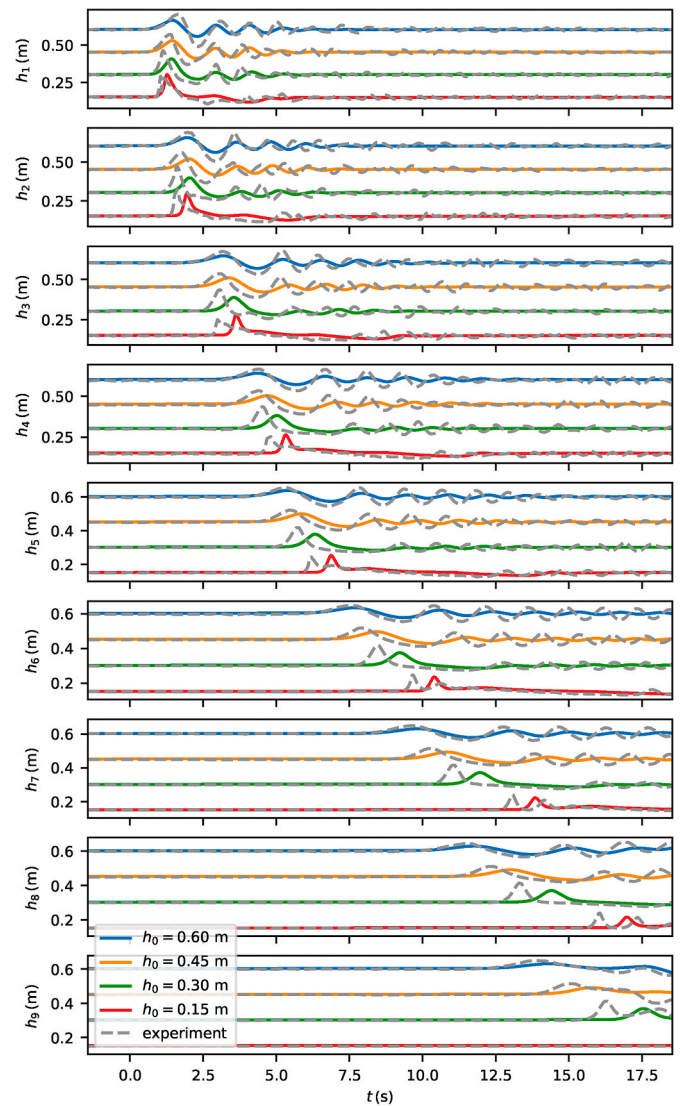

Fig. 16. Wave at gauges in simulations (colour) and experiments (grey) with a landslide volume of $V_0 = 0.1$ m^3. (For interpretation of the references to colour in this figure legend, the reader is referred to the Web version of this article.)

process. Our findings suggest that the landslide mass M (or volume) has a first order effect on the tsunami generation and that the displaced water volume in the basin is the primary factor controlling the tsunami generation. Further, the scaling can be improved by including the Froude number F, indicating that the momentum transfer between the landslide and the water reservoir plays a secondary but still notable role. We anticipate that non-linear effects in the generation phase are also the reason for the non-linear best fit relationship. Combining more than two parameters does not improve the predictive skill of the semi-empirical relations substantially in our case. We further note that there is no substantial difference between sub-critical (F < 1) and critical (F > 1) landslides (see Fig. 14a). A possible reason is that the present configuration resembles a horizontal displacement or pushing rather than a changing bottom topography that moves independently from the wave, such as for submarine landslides (e.g. Løvholt et al., 2015). Moreover, all of the simulations involve supercritical generation in the shallow region of the impact near the shoreline, which implies that the definition of the Froude number in terms of the terminal depth is somewhat artificial. Finally, it should be noted that these observations are limited to idealized water slides and that granular or buoyant slides might behave different.
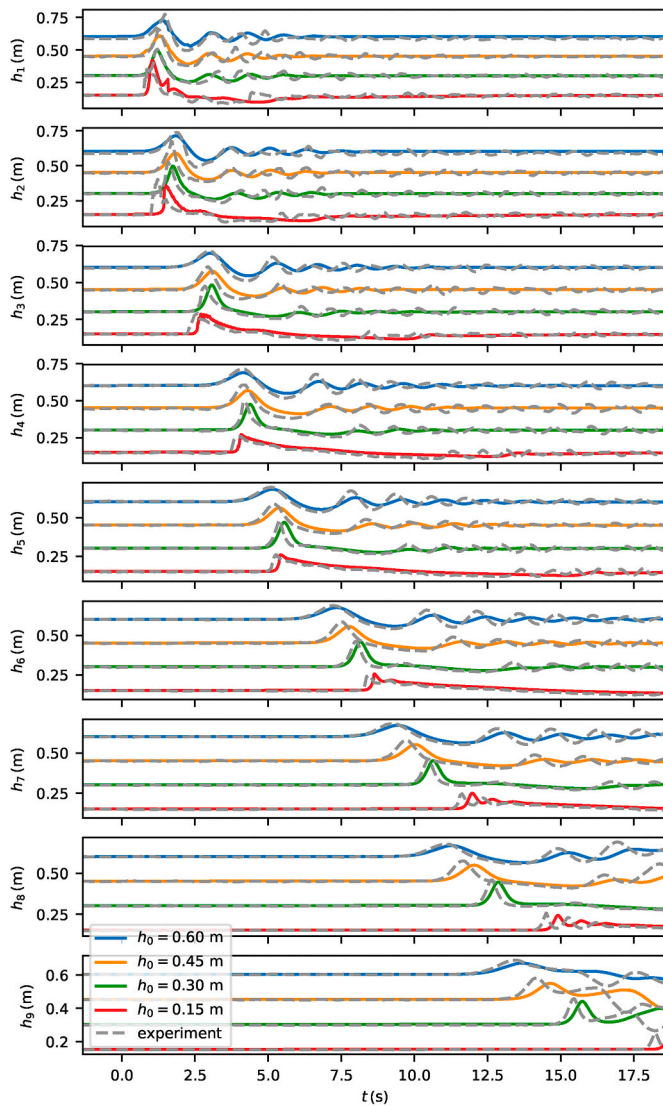
Fig. 17. Wave at gauges in simulations (colour) and experiments (grey) with a landslide volume of $V_0 = 0.2 \text{ m}^3$. (For interpretation of the references to colour in this figure legend, the reader is referred to the Web version of this article.)

Fig. 18. Wave at gauges in simulations (colour) and experiments (grey) with a landslide volume of $V_0 = 0.3 \text{ m}^3$. (For interpretation of the references to colour in this figure legend, the reader is referred to the Web version of this article.)

6. Conclusion and outlook

The experiments of Bullard et al. (2019) allowed us to verify and validate OpenFOAM for landslide tsunamis. The landslide was represented in an idealized manner by water, allowing us to ignore granular rheology and porosity of the landslide. Furthermore, we ignored variations across the tank width to reduce the experiments to a two-dimensional problem. The multiphase solver of OpenFOAM (OpenCFD, 2018; Weller et al., 1998) is well suited to simulate the process, if the correct Courant-Friedrichs-Lewy criterion is considered. However, the CFL criterion is often used in a simplified form, which we found to be insufficient for impulse wave simulations. The strict stability criterion that we applied leads to a substantial increase in computational cost, especially for fine meshes. The applied CFL criterion can be further refined by taking into account that a part of the viscous term is included implicitly. In the long term, an implicitly block-coupled solver (e.g. Uroić et al., 2019), not limited by such a stability condition, is desired to solve these performance issues. In real scale cases this stability criterion might be less problematic due to its scaling with cell size and viscosity. This indicates that the numerical cost of real scale impulse wave cases (as conducted with other tools before, see e.g. Gisler et al., 2006; Gabl
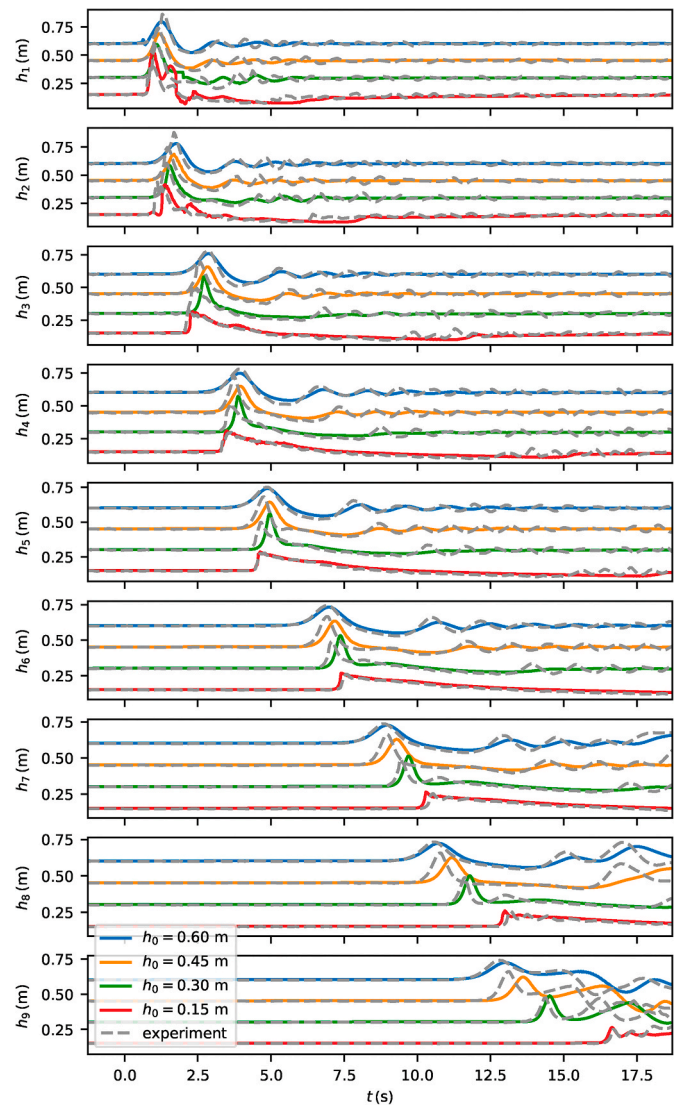
et al., 2015) with OpenFOAM might be manageable. The cell size at the free surface should be smaller than $1/10$ of the expected wave amplitude (see also Roenby et al., 2017). Geometric interface convection schemes (see e.g. Marschall et al., 2012; Roenby et al., 2017) might achieve the same accuracy with less cells. The required grid resolution is achievable for impulse waves with relatively high wave amplitudes (in relation to the simulation domain). However, tsunamis with small amplitude in relation to the simulation domain are out of the scope of this method and depth-integrated models should be applied. The landslide and especially its thin tail and its bottom boundary layer could not be properly resolved in this study, leading to an underestimation of the flow thickness in the tsunamigenic part of the landslide. The slide velocity was not affected, presumably because the boundary layer and basal friction played a minor role in the investigated setup. A more realistic representation of the landslide with complex rheologies might require a substantially higher resolution of the landslide slope.

We executed a sensitivity and scaling analysis in order to evaluate the predictive power of semi-empirical scaling relations. We found that a simple scaling relation involving solely the landslide mass or volume performs surprisingly well. This can be traced back to the wave generation process which relies to leading order on the displacement of water
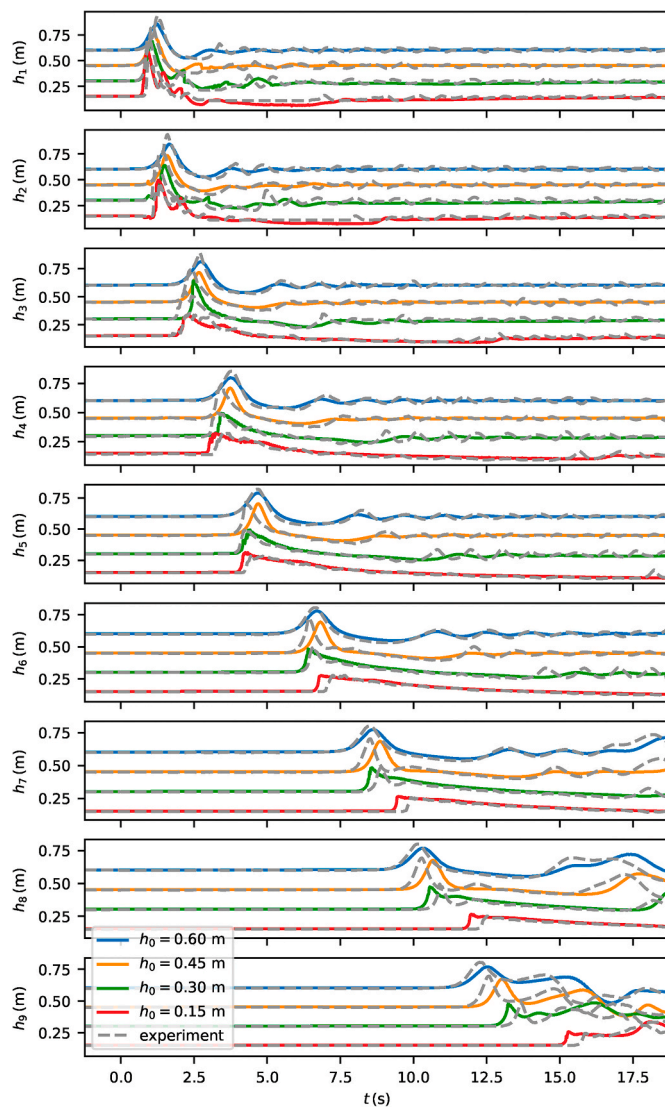
Fig. 19. Wave at gauges in simulations (colour) and experiments (grey) with a landslide volume of $V = 0.4$ m. (For interpretation of the references to colour in this figure legend, the reader is referred to the Web version of this article.)

in the basin. The sensitivity study revealed an upper limit of the tsunami generation duration, after which the first wave crest cannot be influenced by the landslide. In most cases the landslide duration is not sufficient for the wave to run away and the Froude number, quantifying this effect, has less influence compared to submarine landslides. Including the Froude number and thus the landslide velocity into the semi-empirical relation gives a slightly better correlation, which implies a second order effect of momentum transfer from the landslide into the

water reservoir. Furthermore, multi-parameter scaling relations involving three or more landslide parameters did not notably improve the predictive power of the semi-empirical relations. However, this observation is limited to the simplified model applied in here and might not translate to granular and buoyant slides. We noticed that scaling relations based on the total landslide mass cannot easily be transferred between our two simulation setups, which we relate to a more efficient wave generation in the second setup. The scaling relation based on the Froude number and the slide thickness performed better in this regard and achieved good results in both setups with a single set of parameters. However, Froude number and slide thickness are significantly harder to identify and to predict than the total landslide mass.

The applied numerical method is flexible and allows a wide range of further studies. Three dimensional cases and real scale cases are in the range of possibilities with high performance computing. Dynamic mesh refinement and load balancing might further increase the efficiency (Rettenmaier et al., 2019). Granular and other visco-plastic rheologies can be included in a simple way by introducing a non-Newtonian viscosity relation (e.g. Rauter et al., 2020). Porosity and pore fluid effects, on the other hand, require deeper modification of the numerical method (e.g. Cheng et al., 2017; Si et al., 2018b). Natural terrain can be included in simulations with complex body-fitted meshes (e.g. Rauter et al., 2018).

Author statement

Declaration of competing interest

The authors declare that they have no known competing financial interests or personal relationships that could have appeared to influence the work reported in this paper.

Acknowledgements

Appendix A. Stability and time stepping

Hyperbolic equations (2) and (3) introduce characteristic velocities at which disturbances are propagated and the numerical method has to account for this properties. The elliptical pressure equation derived from Eq. (1) is exempted as it is solved implicitly. The characteristic velocity of the momentum conservation equation (3) is usually the highest and introduces the strongest limitations in terms of time step duration. We will show in the following the derivation of the maximum time step duration at which stability can be guaranteed. For the presented simulations, it was imperative to consider the exact limit and not the approximation that is usually applied in OpenFOAM. Equation (3) can be written in a simplified partially dis-cretized form as (see, e.g., Moukalled et al., 2016)

$$V_P \, \rho_P^{i-1} \, \frac{\mathbf{u}_P^i - \mathbf{u}_P^{i-1}}{\Delta t} + \underbrace{\sum_{\forall f} \left(\rho_f^{i-1} \, S_f \, \mathbf{n}_f \cdot \mathbf{u}_f^{i-1} \right) \mathbf{u}_f^{i-1}}_{\text{convective term}} = \underbrace{\sum_{\forall f} \mu_f \frac{\mathbf{u}_N^{i-1} - \mathbf{u}_P^{i-1}}{d_{PN}} S_f + V_P \left(\nabla \cdot \left(\mu \left(\nabla \mathbf{u} \right)^T \right) \right)_P}_{\text{diffusive term}} - V_P \left(\nabla p \right)_P + V_P \, \rho_P^{i-1} \, \mathbf{g}, \tag{41}$$

where the index f indicates values on a face f which is located between cells P and N (see Fig. 15). Face values are calculated by interpolating values on cell centres P and N. The contributions of molecular and turbulent viscosity have been combined into the viscosity μ as their effect on stability is similar. The velocity at the face $\mathbf{u}_f$ is in the following approximated with the upwind scheme for an outward pointing velocity vector as $\mathbf{u}_f = \mathbf{u}_P$. It can be shown that this is the worst case in terms of transient stability and thus an upper limit for the stability criterion. $\mathbf{n}_f$ is the outward pointing (from P to N) face normal vector and S_f the face area. V_P is the cell volume of cell P and d_{PN} is the distance between cell centres P and N.

The index i indicates fields at the unknown time step t^i, the index $i-1$ at the last known time step $t^{i-1} = t^i - \Delta t$, where Δt is the time step duration (see Fig. 15). Discretisation of the pressure gradient term is not required at this point. Furthermore, the transposed component of the viscous term is ignored for simplicity (note that this would be accurate for constant viscosity) and it is assumed that its magnitude matches its non-transposed part, which can be written as a diffusion term. It is further assumed that the diffusion term is included explicitly, although only the transposed component of the viscous term is included explicitly in OpenFOAM. This way, we can estimate the limitation introduced by the transposed component. The stability of transient cases depends on the coefficients of $\mathbf{u}_P^i$ and $\mathbf{u}_P^{i-1}$ in this equation, which are collected and written as a_P^i and a_P^{i-1}. For the solution to be stable and converging, it is required that a_P^i and a_P^{i-1}, i.e. coefficients of temporal neighbours, have different signs (opposite signs rule, see e.g. Moukalled et al., 2016). All coefficients of $\mathbf{u}_P^i$,

$$a_P^i = \frac{V_P \, \rho_P^{i-1}}{\Delta t} > 0, \tag{42}$$

are strictly positive, implying that coefficients of $\mathbf{u}_P^{i-1}$

$$a_P^{i-1} = \frac{V_P \, \rho_P^{i-1}}{\Delta t} - \sum_{\forall f} \left(\rho_f^{i-1} \, S_f \, \mathbf{n}_f \cdot \mathbf{u}_f^{i-1} \right) - \sum_{\forall f} \mu_f \frac{S_f}{d_{PN}} \leq 0 \tag{43}$$

have to be negative for a stable solution. This imposes a restriction on the time step duration Δt,

$$\Delta t \leq \frac{V_P \, \rho_P^{i-1}}{\sum_{\forall f} \left(\rho_f^{i-1} \, S_f \, \mathbf{n}_f \cdot \mathbf{u}_f^{i-1} + \mu_f \frac{S_f}{d_{PN}} \right)}, \tag{44}$$

which is generally known as the CFL condition (after Courant et al., 1928). The Courant-number for equation (41) is defined as

$$\mathrm{CFL} = \frac{\Delta t \sum_{\forall f} \left(\rho_f^{i-1} \, S_f \, \mathbf{n}_f \cdot \mathbf{u}_f^{i-1} + \mu_f \frac{S_f}{d_{PN}} \right)}{V_P \, \rho_P^{i-1}}, \tag{45}$$

and limited to a specific value for stability, in case of the forward Euler scheme, $\mathrm{CFL} \leq 1$ (Moukalled et al., 2016). Contributions of diffusion or viscosity (containing μ) and convection (containing $\mathbf{u}$) are simple to identify and two limit cases of neglectable viscosity

$$\mathrm{CFL}^{\mathrm{conv}} = \frac{\Delta t \sum_{\forall f} \left(\rho_f^{i-1} \, S_f \, \mathbf{n}_f \cdot \mathbf{u}_f^{i-1} \right)}{V_P \, \rho_P^{i-1}}, \tag{46}$$

and neglectable convection

$$\mathrm{CFL}^{\mathrm{diff}} = \frac{\Delta t \sum_{\forall f} \left(\mu_f \frac{S_f}{d_{PN}} \right)}{V_P \, \rho_P^{i-1}}, \tag{47}$$

can be found. The latter is similar to the Fourier number in heat conduction problems (Incropera et al., 2007). Equations can be simplified for one-dimensional equidistant (Δx) grids ($V_P = \Delta x \, \Delta y \, \Delta z$, $S_f = \Delta y \, \Delta z$, $d_{PN} = \Delta x$) and constant fields to Eqs. (11) and (12), which are commonly known and simpler to interpret. However, it should be noted that neither of those should be called Courant-number of Eq. (41), as they only cover respective parts or limit cases. If the viscosity μ is constant, it is possible to implicitly consider the respective term in a segregated solving routine, and only the non-linear convective term has to be considered in the stability criterion (Eq. (46)). Furthermore, assuming flowing water with a velocity of $10 \, \mathrm{m \, s^{-1}}$, the contribution of viscosity would only be relevant for very fine meshes with grid size $\Delta x < 10^{-6}$ m. Therefore, the contribution of viscosity is often neglected, which is also the case in OpenFOAM. However, considering high viscosity flows (e.g. landslides) or flows with low particle velocities (e.g. surface waves), this leads to instabilities with devastating consequences for results. The here investigated flows have a remarkably high turbulent viscosity and a relatively low convection (velocity) in the later stages of wave propagation. Furthermore, small cells are required to describe the free surface waves. All these circumstances lead to a notable contribution of viscosity to the CFL-number and the full relation has to be considered.

Appendix B. Validation simulations

In the following (Figs. 16–19), we will provide the wave gauge data of all 16 simulations, that have been conducted for validation of the numerical routine. These simulations give a good overview over accuracy of the mathematical model and the numerical solution in various situations. This wave gauge data has been summarized in Fig. 8 in form of the first wave crest.

References

Abadie, S.M., Harris, J.C., Grilli, S.T., Fabre, R., 2012. Numerical modeling of tsunami waves generated by the flank collapse of the Cumbre Vieja volcano (La Palma, Canary Islands): Tsunami source and near field effects. J. Geophys. Res. 117 https://doi.org/10.1029/2011JC007646.

Abadie, S., Morichon, D., Grilli, S., Glockner, S., 2010. Numerical simulation of waves generated by landslides using a multiple-fluid Navier–Stokes model. Coast Eng. 57, 779–794. https://doi.org/10.1016/j.coastaleng.2010.03.003.

Barker, T., Schaeffer, D.G., Shearer, M., Gray, J.M.N.T., 2017. Well-posed continuum equations for granular flow with compressibility and µ(I)-rheology. Proc. R. Soc. A 473, 20160846. https://doi.org/10.1098/rspa.2016.0846.

Boyer, F., Guazzelli, É., Pouliquen, O., 2011. Unifying suspension and granular rheology. Phys. Rev. Lett. 107, 188301. https://doi.org/10.1103/PhysRevLett.107.188301.

Bullard, G.K., Mulligan, R.P., Carreira, A., Take, W.A., 2019. Experimental analysis of tsunamis generated by the impact of landslides with high mobility. Coast Eng. 152, 103538. https://doi.org/10.1016/j.coastaleng.2019.103538.

Chen, F., Heller, V., Briganti, R., 2020. Numerical modelling of tsunamis generated by iceberg calving validated with large-scale laboratory experiments. Adv. Water Resour. 142, 103647. https://doi.org/10.1016/j.advwatres.2020.103647.

Cheng, Z., Hsu, T.J., Calantoni, J., 2017. SedFoam: A multi-dimensional Eulerian two-phase model for sediment transport and its application to momentary bed failure. Coast Eng. 119, 32–50. https://doi.org/10.1016/j.coastaleng.2016.08.007.

Courant, R., Friedrichs, K., Lewy, H., 1928. Über die partiellen Differenzengleichungen der mathematischen Physik. Math. Ann. 100, 32–74.

Domnik, B., Pudasaini, S.P., Katzenbach, R., Miller, S.A., 2013. Coupling of full two-dimensional and depth-averaged models for granular flows. J. Non-Newtonian Fluid Mech. 201, 56–68. https://doi.org/10.1016/j.jnnfm.2013.07.005.

Ferziger, J.H., Perić, M., 2002. Computational Methods for Fluid Dynamics, 3 ed. Springer.

Fritz, H.M., 2002. Initial phase of landslide generated impulse waves. Ph.D. thesis. ETH Zurich. https://doi.org/10.3929/ethz-a-004443906.

Gabl, R., Seibl, J., Gems, B., Aufleger, M., 2015. 3-D numerical approach to simulate the overtopping volume caused by an impulse wave comparable to avalanche impact in a reservoir. Nat. Hazards Earth Syst. Sci. 15, 2617–2630. https://doi.org/10.5194/nhess-15-2617-2015.

George, D.L., Iverson, R.M., Cannon, C.M., 2017. New methodology for computing tsunami generation by subaerial landslides: application to the 2015 Tyndall Glacier landslide, Alaska. Geophys. Res. Lett. 44, 7276–7284. https://doi.org/10.1002/2017GL074341.

Gisler, G., Weaver, R., Gittings, M.L., 2006. SAGE calculations of the tsunami threat from La Palma. Sci. Tsunami Hazards 24, 288–312.

Grilli, S.T., Tappin, D.R., Carey, S., Watt, S.F.L., Ward, S.N., Grilli, A.R., Engwell, S.L., Zhang, C., Kirby, J.T., Schambach, L., Muin, M., 2019. Modelling of the tsunami from the December 22, 2018 lateral collapse of Anak Krakatau volcano in the Sunda Straits, Indonesia. Sci. Rep. 9 https://doi.org/10.1038/s41598-019-48327-6, 11946–11946.

Gylfadóttir, S.S., Kim, J., Helgason, J.K., Brynjólfsson, S., Höskuldsson, Á., Jóhannesson, T., Harbitz, C.B., Løvholt, F., 2017. The 2014 Lake Askja rockslide-induced tsunami: Optimization of numerical tsunami model using observed data. J. Geophys. Res.: Oceans 122, 4110–4122. https://doi.org/10.1002/2016JC012496.

Harbitz, C.B., Løvholt, F., Bungum, H., 2014. Submarine landslide tsunamis: how extreme and how likely? Nat. Hazards 72, 1341–1374. https://doi.org/10.1007/s11069-013-0681-3.

Heinrich, P., 1992. Nonlinear water waves generated by submarine and aerial landslides. J. Waterw. Port, Coast. Ocean Eng. 118, 249–266. https://doi.org/10.1061/(ASCE)0733-950X(1992)118:3(249).

Heller, V., Bruggemann, M., Spinneken, J., Rogers, B.D., 2016. Composite modelling of subaerial landslide–tsunamis in different water body geometries and novel insight into slide and wave kinematics. Coast Eng. 109, 20–41. https://doi.org/10.1016/j.coastaleng.2015.12.004.

Heller, V., Hager, W.H., 2010. Impulse product parameter in landslide generated impulse waves. J. Waterw. Port, Coast. Ocean Eng. 136, 145–155. https://doi.org/10.1061/(ASCE)WW.1943-5460.0000037.

Heller, V., Hager, W.H., Minor, H.-E., 2008. Scale effects in subaerial landslide generated impulse waves. Exp. Fluid 44, 691–703. https://doi.org/10.1007/s00348-007-0427-7.

Ilstad, T., Marr, J.G., Elverhøi, A., Harbitz, C.B., 2004. Laboratory studies of subaqueous debris flows by measurements of pore-fluid pressure and total stress. Mar. Geol. 213, 403–414. https://doi.org/10.1016/j.margeo.2004.10.016.

Incropera, F.P., Lavine, A.S., Bergman, T.L., DeWitt, D.P., 2007. Fundamentals of Heat and Mass Transfer. Wiley.

Issa, R.I., 1986. Solution of the implicitly discretised fluid flow equations by operator-splitting. J. Comput. Phys. 62, 40–65. https://doi.org/10.1016/0021-9991(86)90099-9.

Jasak, H., 1996. Error Analysis and Estimation for the Finite Volume Method with Applications to Fluid Flows. Ph.D. thesis. Imperial College, University of London.

Jop, P., Forterre, Y., Pouliquen, O., 2006. A constitutive law for dense granular flows. Nature 441, 727–730. https://doi.org/10.1038/nature04801.

Juretić, F., 2015. cfMesh User Guide. Technical Report. Creative Fields, Zagreb.

Kim, G.-B., Cheng, W., Sunny, R.C., Horrillo, J.J., McFall, B.C., Mohammed, F., Fritz, H. M., Beget, J., Kowalik, Z., 2020. Three dimensional landslide generated tsunamis: Numerical and physical model comparisons. Landslides 17, 1145–1161. https://doi.org/10.1007/s10346-019-01308-2.

Launder, B.E., Spalding, D.B., 1974. The numerical computation of turbulent flows. Comput. Methods Appl. Mech. Eng. 3, 269–289. https://doi.org/10.1016/0045-7825(74)90029-2.

Liu, P.L.-F., Wu, T.-R., Raichlen, F., Synolakis, C.E., Borrero, J.C., 2005. Runup and rundown generated by three-dimensional sliding masses. J. Fluid Mech. 536, 107–144. https://doi.org/10.1017/S0022112005004799.

Løvholt, F., Lynett, P., Pedersen, G., 2013. Simulating run-up on steep slopes with operational boussinesq models; capabilities, spurious effects and instabilities. Nonlin. Processes Geophys. 20, 379–395. https://doi.org/10.5194/npg-20-379-2013.

Løvholt, F., Pedersen, G., 2009. Instabilities of Boussinesq models in non-uniform depth. Int. J. Numer. Methods Fluid. 61, 606–637. https://doi.org/10.1002/fld.1968.

Løvholt, F., Pedersen, G., Gisler, G., 2008. Oceanic propagation of a potential tsunami from the La Palma Island. J. Geophys. Res.: Oceans 113. https://doi.org/10.1029/2007JC004603.

Løvholt, F., Pedersen, G., Harbitz, C.B., Glimsdal, S., Kim, J., 2015. On the characteristics of landslide tsunamis. Phil. Trans. R. Soc. A. 373, 20140376. https://doi.org/10.1098/rsta.2014.0376.

Ma, G., Kirby, J.T., Hsu, T.-J., Shi, F., 2015. A two-layer granular landslide model for tsunami wave generation: Theory and computation. Ocean Model. 93, 40–55. https://doi.org/10.1016/j.ocemod.2015.07.012.

Marschall, H., Hinterberger, K., Schüler, C., Habla, F., Hinrichsen, O., 2012. Numerical simulation of species transfer across fluid interfaces in free-surface flows using OpenFOAM. Chem. Eng. Sci. 78, 111–127. https://doi.org/10.1016/j.ces.2012.02.034.

Mintgen, F., Manhart, M., 2018. A bi-directional coupling of 2D shallow water and 3D Reynolds-averaged Navier–Stokes models. J. Hydraul. Res. 56, 771–785. https://doi.org/10.1080/00221686.2017.1419999.

Moukalled, F., Mangani, L., Darwish, M., 2016. The Finite Volume Method in Computational Fluid Dynamics. Springer. https://doi.org/10.1007/978-3-319-16874-6.

Mulligan, R.P., Franci, A., Celigueta, M.A., Take, W.A., 2020. Simulations of landslide wave generation and propagation using the Particle Finite Element Method. J. Geophys. Res.: Oceans 125, e2019JC015873. https://doi.org/10.1029/2019JC015873.

Mulligan, R.P., Take, W.A., 2017. On the transfer of momentum from a granular landslide to a water wave. Coast Eng. 125, 16–22. https://doi.org/10.1016/j.coastaleng.2017.04.001.

OpenCFD, 2018. OpenFOAM User Guide. OpenFOAM Foundation last checked: 11.08.20. https://sourceforge.net/projects/openfoam/files/v1806/UserGuide.pdf.

Panizzo, A., De Girolamo, P., Di Risio, M., Maistri, A., Petaccia, A., 2005. Great landslide events in Italian artificial reservoirs. Nat. Hazards Earth Syst. Sci. 5, 733–740. https://doi.org/10.5194/nhess-5-733-2005.

Paris, A., Okal, E.A., Guérin, C., Heinrich, P., Schindelé, F., Hébert, H., 2019. Numerical Modeling of the June 17, 2017 Landslide and Tsunami Events in Karrat Fjord, West Greenland. Pure Appl. Geophys. 176, 3035–3057. https://doi.org/10.1007/s00024-019-02123-5.

Pastor, M., Herreros, I., Merodo, J.A.F., Mira, P., Haddad, B., Quecedo, M., González, E., Alvarez-Cedrón, C., Drempetic, V., 2009. Modelling of fast catastrophic landslides and impulse waves induced by them in fjords, lakes and reservoirs. Eng. Geol. 109, 124–134. https://doi.org/10.1016/j.enggeo.2008.10.006.

Rauter, M., Barker, T., Fellin, W., 2020. Granular viscosity from plastic yield surfaces: The role of the deformation type in granular flows. Comput. Geotech. 122, 103492. https://doi.org/10.1016/j.compgeo.2020.103492.

Rauter, M., Kofler, A., Huber, A., Fellin, W., 2018. faSavageHutterFOAM 1.0: depth-integrated simulation of dense snow avalanches on natural terrain with OpenFOAM. Geosci. Model Dev. (GMD) 11, 2923–2939. https://doi.org/10.5194/gmd-11-2923-2018.

Rettenmaier, D., Deising, D., Ouedraogo, Y., Gjonaj, E., De Gersem, H., Bothe, D., Tropea, C., Marschall, H., 2019. Load balanced 2D and 3D adaptive mesh refinement in OpenFOAM. SoftwareX 10, 100317. https://doi.org/10.1016/j.softx.2019.100317.

Roache, P.J., 1997. Quantification of uncertainty in computational fluid dynamics. Annu. Rev. Fluid Mech. 29, 123–160. https://doi.org/10.1146/annurev.fluid.29.1.123.

Roenby, J., Larsen, B.E., Bredmose, H., Jasak, H., 2017. A new volume-of-fluid method in OpenFOAM. In: VII International Conference on Computational Methods in Marine Engineering. Nantes: International Center for Numerical Methods in Engineering.

Romano, A., Lara, J.L., Barajas, G., Di Paolo, B., Bellotti, G., Di Risio, M., Losada, I.J., De Girolamo, P., 2020. Tsunamis generated by submerged landslides: numerical analysis of the near-field wave characteristics. J. Geophys. Res.: Oceans 125, e2020JC016157. https://doi.org/10.1029/2020JC016157.

Rondon, L., Pouliquen, O., Aussillous, P., 2011. Granular collapse in a fluid: role of the initial volume fraction. Phys. Fluids 23, 073301. https://doi.org/10.1063/1.3594200.

Rusche, H., 2002. Computational Fluid Dynamics of Dispersed Two-phase Flows at High Phase Fractions. Ph.D. thesis. Imperial College London.

Savage, S.B., Babaei, M.H., Dabros, T., 2014. Modeling gravitational collapse of rectangular granular piles in air and water. Mech. Res. Commun. 56, 1–10. https://doi.org/10.1016/j.mechrescom.2013.11.001.

Shan, T., Zhao, J., 2014. A coupled CFD-DEM analysis of granular flow impacting on a water reservoir. Acta Mech. 225, 2449–2470. https://doi.org/10.1007/s00707-014-1119-z.

Si, P., Shi, H., Yu, X., 2018a. Development of a mathematical model for submarine granular flows. Phys. Fluids 30, 083302. https://doi.org/10.1063/1.5030349.

Si, P., Shi, H., Yu, X., 2018b. A general numerical model for surface waves generated by granular material intruding into a water body. Coast Eng. 142, 42–51. https://doi.org/10.1016/j.coastaleng.2018.09.001.

Uroić, T., Jasak, H., Rusche, H., 2019. Implicitly Coupled Pressure-Velocity Solver. In: OpenFOAM® Selected Papers of the 11th Workshop. Springer, pp. 249–267.

Versteeg, H.K., Malalasekera, W., 2007. An Introduction to Computational Fluid Dynamics: the Finite Volume Method. Pearson education.

Viroulet, S., Sauret, A., Kimmoun, O., Kharif, C., 2013. Granular collapse into water: toward tsunami landslides. J. Vis. 16, 189–191. https://doi.org/10.1007/s12650-013-0171-4.

Viroulet, S., Sauret, A., Kimmoun, O., Kharif, C., 2016. Tsunami Waves Generated by Cliff Collapse: Comparison Between Experiments and Triphasic Simulations. In: Extreme Ocean Waves. Springer, pp. 173–190.

Ward, S.N., Day, S., 2003. Ritter Island Volcano - lateral collapse and the tsunami of 1888. Geophys. J. Int. 154, 891–902. https://doi.org/10.1046/j.1365-246X.2003.02016.x.

Weller, H., 2006. Bounded Explicit and Implicit Second-Order Schemes for Scalar Transport. Technical Report TR/HGW/06. Nabla Ltd., London, UK.

Weller, H., 2008. A New Approach to VOF-Based Interface Capturing Methods for Incompressible and Compressible Flow. Technical Report TR/HGW/06. Nabla Ltd., London, UK.

Weller, H.G., Tabor, G., Jasak, H., Fureby, C., 1998. A tensorial approach to computational continuum mechanics using object-oriented techniques. Comput. Phys. 12, 620–631. https://doi.org/10.1063/1.168744.

Yavari-Ramshe, S., Ataie-Ashtiani, B., 2016. Numerical modeling of subaerial and submarine landslide-generated tsunami waves–recent advances and future challenges. Landslides 13, 1325–1368. https://doi.org/10.1007/s10346-016-0734-2.

Zitti, G., Ancey, C., Postacchini, M., Brocchini, M., 2015. Impulse waves generated by snow avalanches falling into lakes. In: Proceedings of the 36th IAHR World Congress, the Hague, The Netherlands.